Title: An immunocompetent mouse model of liposarcoma

Amanda M. Shafer[1*], Emma Kenna[2*], Lexi-Ann F. Golden[2*], Ahmed M. Elhossiny[3], Kyle D. Perry[4], Jodi Wilkowski[1], Wei Yan[1], Brynn Kaczkofsky[1], J McGue[1], Scott C. Bresler[4,5,6], Adam H. Courtney[6,7], Jessie M. Dalman[8], Craig J. Galban[9], Wei Jiang[1], Carlos E. Espinoza[1], Rashmi Chugh[10], Matthew K. Iyer[1,3,4,11], Timothy L. Frankel[1], Marina Pasca di Magliano[1], Andrzej A. Dlugosz[5,12], Christina V. Angeles[1,2,5#]

[1]Department of Surgery, University of Michigan, Ann Arbor, MI 48109

[2]Program in Cancer Biology, University of Michigan, Ann Arbor, MI 48109

[3]Department of Computational Medicine and Bioinformatics, University of Michigan, Ann Arbor, MI 48109

[4]Department of Pathology, University of Michigan, Ann Arbor, MI 48109

[5]Department of Dermatology, University of Michigan, Ann Arbor, MI 48109

[6]Rogel Cancer Center, University of Michigan, Ann Arbor, MI 48109

[7]Department of Pharmacology, University of Michigan, Ann Arbor, MI 48109

[8]University of Michigan Medical School, Ann Arbor, MI 48109

[9]Department of Radiology, University of Michigan, Ann Arbor, MI 48109

[10]Department of Internal Medicine, University of Michigan, Ann Arbor, MI 48109

[11]Michigan Center for Translational Pathology, University of Michigan, Ann Arbor, MI 48109

[12]Cell and Developmental Biology, University of Michigan, Ann Arbor, MI, 48109

*Authorship note: AMS, EK, LFG contributed equally to this work and are co-first authors.

Corresponding Author:

Christina V. Angeles, MD, FACS, FSSO

University of Michigan, Rogel Cancer Center

1500 E. Medical Center Drive, 3304 Cancer Center

Ann Arbor, MI 48109

734-615-4823

angelesc@med.umich.edu

Conflict of Interest: C.V.A. receives research funding (to the institution) from Skyline DX. K.D.P receives publishing royalties from Elsevier. The authors declare no relevant competing interests.

ABSTRACT

Liposarcoma (LPS) is the most prevalent soft tissue sarcoma. The most common biological subtypes are well-differentiated (WDLPS), a low-grade disease that can evolve to high-grade dedifferentiated LPS (DDLPS), with increased rates of recurrence and metastasis and low response rates to chemotherapy and targeted therapies. Preclinical testing of immunotherapeutics for LPS has been held back by the lack of an immunocompetent mouse model. Here, we present a spontaneous immunocompetent LPS mouse model, ACPP, with targeted deletion of Trp53 and Pten in adipocytes to mimic signaling alterations observed in human LPS. Similar to human LPS, tumors arising in ACPP mice produce WDLPS and DDLPS, along with tumors that exhibit both WD and DD components. Murine and human DDLPS tumors possess transcriptional similarities, including increased expression of oncogenes Cdk4 and Hmga2 and reduced expression of the tumor suppressor Cebpa; further, both mouse and human DDLPS exhibit either high or low T cell infiltration. Syngeneic cell lines derived from spontaneous ACPP DDLPS reliably produce tumors following orthotopic injection, each with distinct growth patterns, aggressiveness and tumor infiltrating lymphocyte profiles. These models provide much needed tools to understand the complex immunobiology of LPS and greatly accelerate the pace of preclinical studies to uncover new therapies for patients with this aggressive malignancy.

INTRODUCTION

Liposarcoma (LPS) is the most common type of soft tissue sarcoma (STS) and arises in adipose tissues throughout the body. The most common biological types of liposarcoma are well-differentiated (WDLPS) and dedifferentiated liposarcoma (DDLPS). WDLPS, a low-grade disease, can evolve to DDLPS, a high-grade form that is associated with higher rates of local recurrence and distant metastasis (1, 2). WDLPS is treated with surgery alone and has a relatively good prognosis (5-year survival of 85%) (3); in contrast, patients with DDLPS have limited benefit from current systemic treatments. Surgical resection is the most effective treatment option for DDLPS, yet patients have a high risk of recurrence (4). Patients who recur with metastatic disease have poor overall survival of only 12-15 months due to modest response rates to cytotoxic chemotherapy (5, 6). The development of improved systemic therapies for liposarcoma has been limited, leaving our first line therapy, doxorubicin-based chemotherapy, the same since the 1970s (7, 8). Reasons for the lack of progress in

therapeutic development include limited funding for rare disease research and the inability to translate promising preclinical findings from *in vitro* and human xenograft models into effective patient treatments (9, 10).

While immune checkpoint blockade (ICB) immunotherapy has shown tremendous efficacy in many solid tumors, investigation of the immune biology of sarcoma has lagged behind research for other malignancies (11). Recently, however, sarcoma-focused immunology studies have demonstrated links between the tumor immune microenvironment (TIME) and patient outcomes (12-14). One of the first clinical trials, SARC028 (NCT02301039), a phase II, multicenter trial of pembrolizumab, a programmed death 1 (PD-1) checkpoint inhibitor immunotherapy, showed promising activity in select histologic subtypes of advanced soft tissue sarcoma (STS), including DDLPS (15). However, there was only a 20% overall response rate. The causes underlying the limited effect of immunotherapy in DDLPS are poorly understood. Limited data from human samples suggest that improved outcomes are associated with pre-existing immune responses (14, 15). The few DDLPS patients who responded to ICB in SARC028 had pre-treatment tumors with a higher density of effector memory cytotoxic CD8+ T cells (T_{EM}) compared with non-responders (16). These tumors also contained tertiary lymphoid structures (TLS), an ectopic lymphoid structure with T-cell and B-cell rich regions (17). This suggests that productive immune responses occurred in at least a limited group of patients. While this is encouraging, in order to understand what underlies immune responses in patients who benefit from immunotherapy, it is crucial to understand the LPS TIME.

Genetically engineered mouse models (GEMMs) are critical to preclinical immuno-oncology (18). Using GEMMs, we can study mechanisms of action in the context of relevant genetic drivers; further, tumors in these models develop with a stroma and microenvironment that more dependably mimic human disease than cell-line derived models (19). Currently, immunotherapeutics for LPS remain untested *in vivo* due to the lack of a reliable immunocompetent LPS model. In this study we generated and validated a GEMM that carries key genetic aberrations found in human WDLPS/DDLPS. WDLPS and DDLPS are characterized by amplification of chromosome 12q13-15, which contains the major proto-oncogenes murine double minute 2 (*MDM2*) and cyclin-dependent kinase 4 (*CDK4*) (20). *MDM2* is a negative regulator of the tumor suppressor p53, and *CDK4* plays a crucial role in the control of cell cycle progression (9, 21, 22). While over 90% of WDLPS and DDLPS cases show copy number amplification of *MDM2* and ensuing increased proteins levels, expression of *CDK4* is less

consistent (23). Additionally, about 7% of human WDLPS/DDLPS have a *TP53* mutation. While WDLPS and DDLPS are genomically similar, histopathological and clinical differences distinguish them. Human tumors frequently have both DDLPS and WDLPS components, and since they are defined by the highest grade detected, are classified as DDLPS. Conditional inactivation of PTEN and p53 in mice with an adenovirus expressing Cre recombinase (Ad5CMV/Cre) has been shown to lead to the development of multiple types LPS (24). While PTEN mutations are not routinely found in human LPS (20), ~80% of DDLPS have phosphorylated AKT (25). Knocking out *Pten* mimics the effect of constitutive phosphatidylinositol-3-kinase (PI3K)-AKT signaling. *MDM2* amplification is mimicked by knocking out its target operator p53. In order to generate a reliable, spatially restricted LPS mouse model, we designed an adipocyte promoter-driven Cre fusion molecule and used an adenovirus-associated virus (AAV8) vector that elicits minimal immune response (26-28). Here, we characterize the spontaneous AAV8-**A**p2.2/**C**re ***P**ten*$^{f/f}$*;Tr**p**53*$^{f/f}$ C57BL/6 LPS model, hereafter called ACPP, including the histology, genomics, transcriptomics, and immune microenvironment of LPS tumors. We found both low grade WDLPS and high grade DDLPS that exhibited histologic features and gene expression profiles similar to human LPS. Moreover, like human tumors, many murine DDLPS tumors showed an associated WDLPS component. Strikingly, like the human DDLPS tumors observed in the SARC028 trial translational analyses (16), we found 20% of spontaneous ACPP tumors with high tumor infiltrating lymphocytes (TILs). The majority of high TIL tumors were macrophage rich with lower T cell infiltrates. We created 3 syngeneic DDLPS cells lines of variable aggressiveness based on histological features and correlative growth rates, each with consistent orthotopic engraftment. This preclinical model will be an important tool for the sarcoma research community to investigate the mechanism of combination therapies and novel immune-oncology treatment approaches.

RESULTS

Targeted deletion of Trp53 and Pten in adipocytes yields murine liposarcoma histologically similar to human liposarcoma. We sought to create a fully immunocompetent spontaneous GEMM that would produce LPS tumors as a pre-clinical model that recapitulates hallmarks of human LPS. We designed a viral construct using an adipocyte-specific *adiponectin* promoter (mAP2.2) (26) to drive an GFP-Myc tag-Cre fusion molecule (29, 30) (Figure 1A). We then packaged this construct into an AAV8 vector, which effectively transduces adipocytes and induces a negligible immune response (26-28). We confirmed transduction of adipocytes and Cre recombination

after injecting AAV8-Ap2.2-eGFP/Cre (two doses, $1x10^{10}$ vector genomes (vg) or $1x10^{11}$ vg) into the flank fat pad of *mT/mG* reporter mice, which express a constitutive membrane-targeted tdTomato transgene and STOP sequence that are excised by Cre recombinase resulting in a switch to expression of membrane-targeted green fluorescent protein (mtGFP) (Supplemental Figure 1). There was loss of tdTomato and robust mtGFP expression in the adipocytes at the injection site. Although GFP fluorescence could be attributed to viral GFP/Cre expression, membrane localization coupled with loss of tdTomato is consistent with successful Cre-mediated recombination to yield the expected reporter switch. No difference in GFP expression for different doses of virus was observed. We found sparse cells with mtGFP expression in the adjacent interscapular fat pad, and no expression in the lung, similar to the control without injection (Supplemental Figure 1). These data are consistent with successful transduction, resulting in Cre-mediated recombination.

In order to replicate the MDM2 amplification and p53 suppression observed in human LPS (20), we crossed C57BL/6J-congenic *Trp53*^{flox} mice with C57BL/6J-congenic *Pten*^{flox} mice to achieve *Trp53* and *Pten* knockout and thereby mimic the constant activation of AKT seen in up to 80% of human LPS tumors (22, 25). Mice were crossed for multiple generations to establish homozygous *Trp53*$^{f/f}$*Pten*$^{f/f}$ with a C57BL/6 background. We injected AAV8-Ap2.2-eGFP/Cre into bilateral flanks of *Trp53*$^{f/f}$*Pten*$^{f/f}$ C57BL/6J mice, hereby called ACPP (Adipocyte-Cre P53/Pten) (n = 53 total; n = 24 male and n = 29 female) (Figure 1B). LPS penetrance was 76% (80 tumors/106 injections), without evidence of sex differences (77% in males and 74% in females; P = 0.7278). Following AAV8-Ap2.2-eGFP/Cre injections, spontaneous ACPP tumors developed at around 3 months, with others developing during the subsequent 12 months (Figure 1C). No tumors developed in the 10 wild type (WT) C57BL/6J mice that were injected in bilateral flank fat pads. We identified morphological features consistent with human WDLPS and DDLPS, including some tumors with mixed WD and DD components, similar to what we find in human tumors (Figure 1D; see Table 1 and Supplemental Figure 2, A and B). One DDLPS had a heterologous component of osteosarcomatous (OS) differentiation, analogous to a phenomenon sometimes seen in human DDLPS (Figure 1D, far right panel). Histological analysis of spontaneous ACPP tumors identified 50% WDLPS, 30% mix of WDLPS/DDLPS, and 20% DDLPS (Figure 1E). Mixed WDLPS/DDLPS were grouped with DDLPS for further analysis following standard pathological and clinical classification of these mixed tumors in patients (31). Since mice were injected in bilateral flank fat pads, some tumors were removed at a smaller size if they

grew more slowly than the contralateral tumor, which reached the protocol's maximum size endpoint of 2 cm in diameter. Therefore, there was a significant difference in the median size of histologically different tumors − 288 mm^3 for WDLPS and 1666 mm^3 for DDLPS (Figure 1F; P = 0.0006) − suggesting that ACPP WDLPS could evolve to DDLPS over time, consistent with ongoing genomic instability seen in WDLPS/DDLPS human tumors (32). Immunohistochemical (IHC) staining of representative DDLPS consistently demonstrated lack of desmin expression, thereby eliminating the possibility of a diagnosis of other high-grade myogenic tumors such as leiomyosarcoma (33) (Supplemental Figure 2C). Tumors did not exhibit morphologic features of other liposarcoma variants such as the myxoid stroma of myxoid liposarcoma or pleomorphic lipoblasts of pleomorphic liposarcoma (PLPS) (34), which itself does not exhibit an associated WDLPS component (34). Upon histological review, 26 ACPP samples could not definitively be diagnosed as LPS, and hence, were classified as 'indeterminate' lipomatous tumor, and, therefore, not included in penetrance calculation and excluded from further analysis (Supplemental Figure 2D). All mice in this study reached humane endpoints prior to developing lung or liver metastases, examined both macro- or microscopically. Non-contrasting magnetic resonance imaging (MRI) was used to identify spontaneous ACPP tumors before they were palpable, allowing us to track tumor growth (Figure 1G and Supplemental Figure 3). Therefore, this technique presents the opportunity to begin therapeutic intervention after confirming tumor initiation and growth by MRI, prior to the tumor being palpable.

Multi-omic characterization of ACPP tumors reveals similarities to human LPS. WDLPS and DDLPS are genomically characterized predominantly by many copy number alterations (CNAs). Most prevalent is amplification of chromosome 12q13-15, which contains MDM2 and CDK4, and an overall low tumor mutational burden (20, 35). To understand the biological processes that lead to tumor development in the ACPP model, we performed genomic and transcriptional profiling of murine tumors and compared them to human WDLPS and DDLPS. By whole exome sequencing (WES) of murine tumors (n =14), we detected a low tumor mutational burden and a substantial amount of CNAs, with a higher frequency in DDLPS than WDLPS (Figure 2A), consistent with human LPS (31, 32). Chromosomes 3, 5, and 15 largely had copy number gains, whereas chromosomes 2, 7, and 14 had frequent copy number losses (21, 36, 37) (Figure 2A). In human LPS, transcriptional changes are due primarily to copy number variations rather than genetic mutations (32). Notably, we observed significant copy number losses on murine chromosome 7, which contains CCAAT/enhancer binding

protein alpha (*C/ebpa)*. This transcription factor is crucial for adipose tissue development; it also acts as a tumor suppressor and serves as a master regulator of adipogenic differentiation (38, 39). In human LPS, under-expression of C/EBPA can be due to hypermethylation or allelic loss in 32% of DDLPS patients, and is associated with worse disease-specific survival (31). Our mouse data also demonstrated copy number gains on murine chromosome 5, which contains the gene encoding cyclin-dependent kinase 6 (*Cdk6)*. CDK6 is key for cell cycle progression, and its overexpression in cancer is often linked to uncontrolled tumor growth (40). Interestingly, DDLPS tumors with the most copy number losses throughout chromosome 11 (N1019 and N1692), where the mouse *Trp53* gene is located, had the highest magnitude of *Trp53* loss (Supplemental Figure 4A). Further analysis of CNAs across spontaneous tumors revealed significant differences in fraction of genome altered (FGA) when samples were stratified by histological classification and amount of tumor infiltrating lymphocytes (TILs) in the TIME. WDLPS had a significantly lower FGA compared to DDLPS, with low TILs (WDLPS v DDLPS-low TILs; $P = 0.017$), in keeping with human LPS (31). DDLPS-low TILs had a significantly higher FGA compared to DDLPS-high TILs ($P = 0.024$) (Figure 2B; Supplemental Figure 4B); however, this could be due to low tumor purity resulting from high immune infiltrate. Bulk RNA sequencing (RNA-seq) was conducted to determine gene expression profiles for murine LPS histological subtypes generated by the ACPP model. Differential gene expression (DGE) analysis revealed that WDLPS ($n = 3$) and DDLPS ($n = 10$) had both differentially expressed up- and downregulated genes in comparison to normal fat controls ($n = 4$) (Supplemental Figure 4 C and D). We also performed RNA-seq and DGE analysis on human tumors (WDLPS $n = 8$; DDLPS $n = 8$), pathologically confirmed by STS pathologists, compared to normal fat ($n = 8$). Gene set enrichment analysis (GSEA) showed that upregulated and downregulated gene sets in mouse ACPP DDLPS were transcriptionally similar to human DDLPS, with statistical significance (NES 2.5, padj $2x10^{-50}$ and 2.5, $9.5x10^{-35}$, respectively) (Figure 2C). We did not see the same concordance in WDLPS (Supplemental Figure 4E), likely due to the well-differentiated subtype having more similarity to normal fat with mostly upregulated and minimal downregulated gene differences (Supplemental Figure 4D). Additionally, the ACPP model does not have MDM2 amplification, which is the most differentiating gene in human WDLPS compared to normal fat. Even though the ACPP model is not designed to overexpress *Mdm2*, interestingly, both *Cdk4* and *Hmga2*, which are found on chromosome 10 along with *Mdm2*, were significantly overexpressed in DDLPS tumors (log2 FC 1.1, *P adj.* = 0.002 and 9.8, *P adj.* = $2.9x10^{-9}$, respectively) (Supplemental Figure 4C). In human DDLPS, *CDK4* and *HMGA2*, oncogenes on chromosome 12q

with copy number amplification and overexpression, also drive tumorigenesis (41). Under-expression of *C/EBPa* is important for DDLPS growth in xenograft models and is associated with worse patient survival (36, 42, 43). We also saw under-expression of *C/epa* in murine ACPP DDLPS (Supplemental Figure 4C). Importantly, when comparing murine and human DDLPS against their respective species-specific normal fat, we identified concordance in both significantly upregulated hallmark pathways, including those involved with cellular proliferation (G2M checkpoint and E2F targets) and developmental programs (epithelial to mesenchymal transition), and significantly downregulated pathways, including the adipogenesis pathway and those involved with metabolic programs (fatty acid metabolism and oxidative phosphorylation) (Figure 2D). These findings highlight the transcriptional similarities between human and murine DDLPS, and support the role of the ACPP model as a valuable tool in preclinical applications.

Spontaneous ACPP DDLPS tumors vary in density and composition of TILs. All spontaneous ACPP tumors (n = 80) were initially classified into low, moderate or high TIL status based on the abundance of lymphocytes and their proximity to tumor cells by H&E. High TILs were found in 18% of the DDLPS tumors (Table 1). When evaluated by grade, the grade 2 DDLPS subset had 2.2-fold as many high TIL tumors as grade 3 (30% vs 13%, respectively). DDLPS tumors without a WD component also had higher TIL than those with both WD and DD components (25% vs 13%, respectively). As expected, 85% of WDLPS lacked significant TILs, with none showing high TIL infiltrate (Table 1). These findings recapitulate similar variability in immune infiltration seen in human LPS (16, 17). To characterize the TIME of ACPP tumors, we performed multiplex IHC (mIHC) analysis of immune cell populations, which revealed an overall low level of immune infiltrate in spontaneous ACPP WDLPS tumors (Figure 3A) and two distinct subsets of spontaneous ACPP DDLPS tumors with either low or high levels of TILs, hereby called $DDLPS^{lo}$ or $DDLPS^{hi}$, respectively (Figure 3B-C). The mIHC panel probed for T cell markers $CD3^+$ and $CD8\alpha^+$, regulatory $CD4^+$ marker $FOXP3^+$, checkpoint marker $PD\text{-}1^+$, macrophage marker $F480^+$, and B cell marker $CD19^+$. Specified phenotype immune cells were quantified using InForm analysis (44-46). Spontaneous murine liposarcoma tumors were classified as $DDLPS^{hi}$ if $CD3^+$ T cells out of total cells (determined by nuclear DAPI stain) was $\geq$ 20% and $DDLPS^{lo}$ if < 20% (n = 5 per classification). $DDLPS^{hi}$ tumors had an increase in percentage of $CD3^+$ (Figure 3D), $CD3^+CD8\alpha^+$ (Figure 3E), and $CD3^+CD8\alpha^-FOXP3^+$ Treg (Figure 3F) cells out of total cells in comparison to $DDLPS^{lo}$ (P = 0.0079) and WDLPS (P = 0.0079;). Although

not statistically significant, DDLPS^{hi} tumors trended towards having more CD19^{+} B cells (Figure 3G) and fewer F4/80^{+} macrophages (Figure 3H) compared to DDLPS^{lo} (P = 0.55 and P = 0.55, respectively). Interestingly, while there was not a statistically significant difference in the percent of macrophages between DDLPS^{hi} and DDLPS^{lo}, each subtype produced qualitatively distinct spatial patterns. Macrophage populations in DDLPS^{lo} were diffuse throughout tumors but confined to the periphery of DDLPS^{hi} tumors (Supplemental Figure 5). Gene set variation analysis (GSVA) was performed on bulk RNA-seq from spontaneous murine ACPP LPS tumors (n = 13) and normal fat (n = 4) using signatures defined (47) to quantify immune and stromal cell populations. DDLPS samples with high TILs were differentiated from those with low TILs (Figure 3I). Specifically, DDLPS tumors with high TILs had higher infiltration of T cells, memory B cells, and CD8 T cells compared to both DDLPS with low TILs and normal fat (Figure 3I). However, DDLPS with high TILs showed reduced macrophage infiltration (as determined by monocyte/macrophage enrichment) compared to DDLPS with low TILs but displayed higher macrophage infiltration relative to normal fat (Figure 3I). Altogether, these results emphasize the significant variability in immune cell infiltration within spontaneous ACPP tumors, leading to distinctive TIMEs classified by immune cell population composition and unique spatial immune population patterns.

Intratumoral T cell phenotypes vary significantly among murine LPS histological subtypes. After observing increased infiltration of various T cell populations in DDLPS^{hi} tumors using both mIHC and GSVA, we developed a targeted mIHC panel to investigate resident memory CD8+ T cells (T_{RM}). These cells are known to offer significantly stronger protective immunity in peripheral tissues compared to circulating central memory T cells (T_{CM}) in both tumor and infectious disease models (48-50). Additionally, T_{RM} cells are associated with better outcomes in patients with multiple solid malignancies (51-57). A core set of markers used to identify CD8^{+} T_{RM} include CD69, a key marker that distinguishes memory T cells in tissues from those in circulation, CD103 (ITGAE) an adhesion protein expressed by a subset of tissue memory CD8^{+} T cells, and PD-1, an inhibitory receptor expressed on CD8^{+} T_{RM} typically associated with prolonged antigen exposure in contexts such as tumors and chronic infections (58-60). Using the T_{RM} mIHC panel, we again found two distinct subsets of DDLPS with considerably different immune spatial patterns (Figure 4, A and B). DDLPS^{hi} tumors had a statistically significant increase in percentages of CD4^{+} (Figure 4C) and CD8α^{+} (Figure 4D) T cells out of total cells in comparison to DDLPS^{lo} and WDLPS (P = 0.0079 and P = 0.036, respectively). CD8^{+}PD1^{+} T cells were significantly reduced in

DDLPS^{hi} tumors versus DDLPS^{lo} tumors (P = 0.037) (Figure 4F), and CD4^{+}PD1^{+} cells trended upward in DDLPS^{lo} tumors versus DDLPS^{hi} (P = 0.55) (Figure 4E). Examination of CD8^{+} T cell subtype distribution by resident memory markers revealed distinct, statistically significant ($P < 2.2e^{-16}$) differences in the proportion composition of CD8^{+} T cell phenotypes among LPS subtypes. WDLPS was mostly comprised of CD69^{+} CD103^{-} PD1^{-} CD8^{+} T cells (Figure 4G). The CD8^{+} T cell phenotypes in DDLPS^{lo} were similar to those in WDLPS, with the largest proportion remaining CD69^{+} CD103^{-} PD1^{-}, but with more CD69^{+} CD103^{-} PD1^{+} (T_{RM}-like) and CD69^{-} CD103^{-} PD1^{+} CD8^{+} T cells (Figure 4G). CD8^{+} T cell phenotypes were considerably different in DDLPS^{hi} compared to DDLPS^{lo} and WDLPS, with the largest T cell population being CD69^{-}CD103^{+}PD1^{+} CD8^{+} T cells, a population not identified in the other subtypes (Figure 4G). While CD69 is a marker of activation, it can be downregulated in chronic infection (61) and cancer (62). DDLPS^{hi} also had a substantial increase in the proportion of CD69^{-}CD103^{+}PD1^{-} CD8^{+} T cells and decreased proportions of CD69^{+}CD103^{-} PD1^{-} CD8^{+} CD69^{+} CD103^{-} PD1^{+} (T_{RM}-like) and CD69^{-} CD103^{-} PD1^{+} CD8^{+} T cells compared to WDLPS and DDLPS^{lo} (Figure 4G). While InForm analysis did not reveal any CD69^{+}CD103^{+} CD8^{+} T_{RM} cells, they were identified by mIHC (Supplemental Figure 6). This finding is attributed to the low abundance of CD69^{+}CD103^{+} CD8^{+} T_{RM} cells, resulting in a reduced likelihood of identification by InForm analysis.These data indicate that, beyond the overall increased T cell infiltration in DDLPS^{hi}, a notable variation in T cell phenotypes likely correlates with the underlying transient anti-tumor response to immunotherapy observed in the few DDLPS patients from the SARC028 trial who had high tumoral T cells (16). This highlights the potential utility of ACPP as a preclinical model for immunotherapeutic testing.

Syngeneic cell lines derived from primary spontaneous ACPP DDLPS produce tumors following orthotopic injection. Syngeneic cell lines to generate tumor-producing allografts or cell line-derived tumors (CLDTs) in immunocompetent mice are efficient and predictable translational models allowing evaluation of immunotherapeutics. Hence, we established cell lines from spontaneous ACPP DDLPS tumors. We generated and tested three syngeneic cell lines (N1011, N1018, and N1343) isolated from three distinct ACPP tumors. All three cell lines originated from grade 3 DDLPS spontaneous tumors and produced fully penetrant DDLPS CLDTs in syngeneic WT C57BL/6J mice (Supplemental Figure 7C). N1343 was created from a spontaneous ACPP tumor with high TILs. The three cell lines showed distinct growth patterns *in vivo* when injected subcutaneously into the flanks of C57BL/6J mice (Figure 5A). N1018 CLDTs were the most aggressive and developed within 7

days of cell line injection. N1011 and N1343 were less aggressive and developed within 49 – 77 days post injection. Attempts to slow the growth of N1018 by reduction of the initial number of cells (2.5e5 vs. 1e6 cells) were unsuccessful, as palpable CLDTs were still evident ~ 7 days post injection. H&E analysis demonstrated morphological characteristics in CLDTs similar to their respective spontaneous ACPP tumors (Figure 5B; Supplemental Figure 7A).

Tail vein injections of DDLPS cell lines results in lung metastasis with only the most aggressive N1018 cell line. Mice with orthotopic CLDTs did not develop visible or microscopic metastases prior to humane endpoint (tumor size = 20 mm in diameter). To assess the metastatic potential of our DDLPS cell lines, WT C57BL/6J mice were injected intravenously (i.v.) through the tail vein with each cell line. Twenty-nine percent of the mice injected with N1018 (*n* = 4 out of 14) developed lung metastasis in an average of 36 days while no mice injected with N1011 or N1343 (*n* = 5 per group). had evidence of lung metastasis over the course of 160 days. All lung tumors demonstrated the same histological characteristics of flank tumors, consistent with a diagnosis of grade 3 DDLPS lung metastases (Figure 5C). There were no liver or other organ sites of metastasis with any cell line, demonstrating similar organotropism as in humans with a predilection of lung metastasis as the most common metastatic site in patients with DDLPS (5, 6).

Adipogenic differentiation gene expression varies among DDLPS cell lines. DDLPS is arrested at an early-stage of adipogenic differentiation (63). To determine the differentiation state of each of the syngeneic cell lines, the gene expression of known adipocyte markers was compared between cell lines and adipocytes in different stages of differentiation. Pre-adipocytes (3T3 cells, day 0) were treated with differentiation factors and collected at early differentiation (day 2) and at late stage with mature adipocytes with lipid droplets (day 9). Syngeneic cell lines showed very low expression of mature adipocytic markers *AdipoQ, Cebpa, Pparg,* and *Fabp4* compared to mature adipocytes (3T3 D9), as well as low levels of *AdipoQ, Pparg,* and *Fabp4* compared to early differentiated adipocytes (3T3 D2) (Figure 5, D-G). Notably, *Cebpa* expression varied across the syngeneic cell lines. N1011 and N1343 showed *Cebpa* levels similar to those in early differentiated adipocytes (3T3 D2), while N1018 had significantly lower *Cebpa* expression, akin to pre-adipocytes (3T3 D0). This reduced expression in N1018 also coincided with the lowest levels of *AdipoQ*, suggesting less differentiation compared to N1011 and N1343 and correlating with the higher aggressiveness of N1018 (Figure 5, D and E).

DDLPS CLDTs have variable TIL profiles. We used a mIHC standard immune panel ($CD3^+$, $CD8\alpha^+$, $FOXP3^+$, $PD1^+$, $F480^+$, and $CD19^+$) to analyze the TIME in CLDTs. We found distinct variations in the proportions of specific immune cell populations among the three CLDTs. N1011 had the highest proportion of macrophages and the lowest frequency of $CD3^+$ T cells within the tumor, whereas N1018 had increased frequency of $CD3^+$ T cells but retained the large, diffuse population of macrophages seen in N1011 (Figure 5H). N1343, which came from a $DDLPS^{hi}$ tumor, had the largest proportion of $CD3^+$ T cells within the tumor, with visual $CD3^+$ T cell aggregates and the lowest visual proportion of $F4/80^+$ macrophages (Figure 5H). N1343 CLDTs did not share the same high TIL profile as the spontaneous tumor it was derived from. This was not surprising, given that syngeneic cell line models typically do not form TLS as cell lines may have evaded immunosurveillance in their original host and the rapid growth does not allow time for TLS organization (19, 64-66). Nonetheless, the diverse TIL profiles among the three CLDTs provide a reliable model for generating DDLPS tumors in immunocompetent mice, facilitating preclinical immunotherapy translational studies.

CLDTs have distinct differences in T cell phenotypes within the TIME. To characterize the TIME, immune populations from all three tumors were analyzed by spectral flow cytometry (n = 5 – 10 per cell line). Samples were selected that were near the median percentage of CD3+ T cells out of CD45+ cells for each cell line (n = 3 per cell line). $CD3^+$ T cell populations were clustered based on our T cell phenotype markers including CD4 and CD8, CD44 for antigen-experienced, CD69 for activation, CD103 and CXCR6 for residency, CD62L for circulation, and checkpoints LAG3 and PD-1 as markers of exhaustion (67).T-distributed stochastic neighbor embedding (t-SNE) analysis was used to compare CD3+ populations between CLDTs (see Supplementary Figure 8A for pre-gating strategy). Using the FlowSOM clustering algorithm (68), we identified 15 CD3+ cell clusters, comprised of $CD4^+$ T cells (red), $CD8^+$ T cells (blue), and $CD4^-/CD8^-$ double negative (DN) populations (grey) (Figure 6A). CD69, CD103, CXCR6, CD44, CD62L, PD-1, LAG3 markers were used to identify populations based on mean fluorescent intensities (MFI) that were mapped to the meta-clusters heat map generated by FlowSOM (Supplemental Figure 9A). We identified naïve T cells, characterized by elevated CD62L and the lack of CD44 and CD69 (69); memory T cells, marked by shared expression of CD44 and CD69; resident-memory T cells (T_{RM}) that expressed CD103 and/or CXCR6; exhausted T cells by the dual expression of PD-1 and LAG3

(67), and DN cells that were CD3+ but lacked both CD8 and CD4 (70) (Figure 9B). The majority of T cells in CLDTs were the memory phenotype. t-SNE plots for CLDTs showed that N1343 (derived from a DDLPS^{hi} ACPP tumor) harbored the most exhausted PD-1+/LAG3+ CD4+ and CD8+ T cells and contained the least naive CD8+ T cells (Figure 6C). Specific populations within CLDTs were also quantified by manual gating (see Supplementary Figure 8, B and C). Overall, N1343 had the highest percentage of CD3$^+$ T cells compared to N1018 (P = 0.023), with no significant differences between N1011 and N1018 (Figure 6D). N1018 had a higher proportion of CD4$^+$ T cells compared to N1343 (P = 0.047) (Figure 6E) but a significantly lower proportion of CD8$^+$ T cells (P = 0.00077) (Figure 6F). We did not find differences in the amount of PD-1+ or LAG3+ CD8+ T cells between CLDTs (Supplemental Figure 10, C and D). CD69+CD8+ T cells was similar in N1011 and N1018, but higher in N1343 compared to N1018 (P = 0.016) (Supplemental Figure 10E). CD103$^+$ CD8$^+$ T cells in N1018 was significantly higher compared to N1343 and trended higher compared to N1011 (P = 0.00028 and P = 0.069, respectively), while there were no differences between N1011 and N1343 (Supplemental Figure 9F). The dual expression of CD69 and CD103 is characteristic of tissue-resident memory (T_{RM}) T cells, which when present are associated with improved response to immunotherapy (67, 71). The most aggressive cell line, N1018, had the highest percentage of CD69$^+$CD103$^+$ CD8$^+$ T_{RM} compared to N1011 and N1343 (P = 0.028 and P = 6.8e-5, respectively) (Figure 6G), suggesting that even though N1018 CLDTs have overall lower CD8+ T cells than N1034, their tumor intrinsic properties may promote a more immunogenic TIME characterized by antitumoral T cell phenotypes, including T_{RM}.

Myeloid populations, including CD11b+ myeloid cells and F4/80+ macrophages, play a critical role in modulating the behavior of lymphocytes in the TME (72). We found no differences in the levels of CD11b$^+$ myeloid cells (Figure 6H) and CD11b$^+$F480$^+$ macrophages (Supplemental Figure 10A) between cell lines. The percentage of F4/80^{hi} expressing macrophages, which is indicative of tumor-associated macrophages (TAMs), was highest in N1343 CLDTs compared to N1011 (P = 0.03) but showed similar levels to N1018 (Figure 6I). The percentage of CD19$^+$ B cells was about two-fold higher in N1343 compared to N1018 and N1011; however, the differences were marginally outside the significance threshold (P = 0.052; P = 0.13) (Supplemental Figure 10B). Overall, these findings highlight the distinct immune landscapes present within each CLDT, with N1343 exhibiting a more exhausted T cell phenotype, and N1018 displaying a more immunogenic TIME characterized by a higher proportion of T_{RM} cells. Despite variations in T cell composition and phenotypes, myeloid and macrophage

populations appeared relatively consistent across all three CLDTs, suggesting that intrinsic tumor properties may play a crucial role in shaping T cell immune responses. With their distinct characteristics, these cell lines used in concert provide a robust framework for investigating mechanisms of immune suppression, thereby laying the groundwork for developing future therapeutic strategies.

DISCUSSION

To the best of our knowledge, this study describes the first spontaneous immunocompetent LPS mouse model that reliably mimics human LPS in several key aspects. First, histopathology of the ACPP tumors shows mice develop both WDLPS and DDLPS tumors in our model, with some tumors exhibiting both WD and DD components, similar to what is seen in patients with LPS (Figure 1D; Supplemental Figure 2, A and B). DDLPS always arises in the context of WDLPS, thereby confirming that our model is WD/DDLPS, and not pleomorphic liposarcoma (31, 32). Second, mouse ACPP DDLPS possesses transcriptional similarities with human DDLPS, including the increased expression of oncogenes *Cdk4* and *Hmga2,* reduced expression of the tumor suppressor *Cebpa* (Supplementary Figure 4C), and concordance in the significantly upregulated and downregulated hallmark pathways (Figure 2, C and D). Third, and most compelling, is the variability in the TIME of the ACPP model, which develops tumors with either high or low T cell infiltration (Figure 3). In the correlative analyses of the SARC028 clinical trial patients, the 20% of DDLPS patients who responded to anti-PD-1 had pre-treatment tumors with a higher density of cytotoxic tumor infiltrating T cells. The ACPP model generates about 18% of DDLPS^{hi} tumors, strikingly similar to the 20% of patients with high T cell tumor infiltrates. The spontaneous ACPP model offers a powerful research tool to investigate the mechanisms of immunosuppression in DDLPS, with the long-term goal to improve immunotherapy approaches for this disease.

Our group and others have shown that the presence of tissue-resident memory T cells (T_{RM}) in the tumor microenvironment plays a significant role in the anti-tumor immune response and predicts better outcomes in patients with multiple solid malignancies (51-57). We found a striking difference in T cell phenotypes in DDLPS^{hi} compared to DDLPS^{lo} murine tumors. DDLPS^{hi} had a higher percentage of CD69^{-}CD103^{+}PD-1^{+} CD8^{+} T cells, indicating a T_{RM}-like population that initially expressed CD69 during early activation but subsequently downregulated it, similar to patterns observed in chronic infection and certain solid tumors (61, 62). We identified only a few CD103^{+}CD69^{+} CD8^{+} T_{RM} cells in DDLPS^{hi} tumors and none in DDLPS^{lo}, suggesting that this is not a predominant T cell phenotype in liposarcoma (Figure 4G, Supplemental Figure 6). Overall, our data emphasize

differences not only in the presence and density of T cells in LPS, but also in the specific phenotypic profiles of the CD8+ T cells necessary for antitumor immunity. Our model can serve as a platform to evaluate new immunotherapy strategies and determine how LPS tumor resident immune cell populations affect treatment outcomes.

Analysis of pre-treatment biopsies from patients with DDLPS who had improved progression-free survival in phase II ICB trials revealed the presence of TLS (14, 15), an ectopic lymphoid structure that consists of T-cell and B-cell rich regions and other immune populations (17). Our data suggest that DDLPS^{hi} tumors likely contain immature TLS, based on observed disorganized aggregates of T and B cells, as well as an increased abundance of exhausted T cells (Figure 3C) (73). This lack of functional immune activity can have different causes, including intrinsic T cell dysfunction or accumulation of immune suppressive myeloid cells (74). Pathological data from over 1,200 sarcoma patients with over 27 histological subtypes, including 62 DDLPS patients, demonstrated infiltration of predominantly pro-tumorigenic tumor-associated macrophages with density that exceeded that of TILs (75, 76). In pancreatic cancer, another “cold,” poorly immunogenic tumor, immunotherapy has largely been ineffective; however, studies of exceptional survivors showed the presence of memory T cells expressing TCRs that recognize tumor antigens, even decades after the primary tumor was resected (77). Thus, even in poorly immunogenic tumors, if the immune system is engaged, long-term immune control of tumors is possible. Developing immunotherapeutic approaches for LPS patients will depend on further investigation of DDLPS^{hi} and DDLPS^{lo} tumors using both spatial and single-cell sequencing, to deepen our understanding of immune interactions that are occurring in high TIL tumors.

We developed three syngeneic cell lines from three independent DDLPS ACPP-derived tumors that demonstrate 100% penetrance as orthotopic allografts in C57BL/6 mice. Syngeneic models are important research tools that develop tumors faster and are less expensive than spontaneous GEMM models; moreover, each cell line enhances reproducibility and exhibits specific traits that allow us to study tumor heterogeneity. In contrast to xenograft models previously used in LPS preclinical studies (36), syngeneic cell line *in vivo* models have an intact immune system, where we can study the TIME and immunotherapies. Each of the ACPP-derived cell lines described herein have distinct growth patterns, aggressiveness and TIL profiles. The most aggressive DDLPS cell line (N1018) is characterized by fast growth, metastatic potential, and the most dedifferentiated phenotype (lowest expression of *Cebpa*, *Pparg*, and *AdipoQ*) (Figure 5), but interestingly, has the highest

population of CD8+ T_{RM} cells (Figure 6). This suggests a TIME that is potentially responsive to immunotherapy; however, the increased abundance of macrophages and other barriers may need to be overcome to prompt a durable response. This highlights the utility of our models for investigating tumor cell-immune interactions in response to therapies, chemotherapy, immunotherapy, and combination therapies in DDLPS cell line allografts in preclinical translational studies.

While ACPP mice and ACPP-derived DDLPS cell line allografts carry key genetic aberrations found in human LPS, a potential limitation is that these models do not have copy number amplification and overexpression of MDM2 found in the majority of human WDLPS and DDLPS tumors. Despite promising preclinical results with MDM2 inhibitors *in vitro* and in patient tumor-derived DDLPS xenografts, including complete tumor regression in some models (10, 78-80), multiple clinical trials have not demonstrated a clear benefit in DDLPS patients (9). This outcome emphasizes the need for improved preclinical models, such as an adipocyte-specific MDM2-overexpressing GEMM that we are currently evaluating. Although preclinical animal models have limitations, developing effective therapies requires leveraging a variety of models. The ACPP mice and cell lines described will allow exploration of the underlying mechanisms affecting how tumor cell and immune microenvironment interact in response to therapy. This approach is especially critical to advancing our understanding and achieving breakthroughs in rare cancers like liposarcoma.

In conclusion, the development and validation of a new, highly penetrant immunocompetent GEMM for spontaneous LPS, along with syngeneic cell lines, offers the sarcoma research community a crucial immunocompetent animal model. Our model closely mimics human disease and holds the potential to greatly accelerate the pace of uncovering new therapies for patients with LPS.

METHODS

Sex as a biological variable. Both male and female mice were used for all experiments and data show similar findings for both sexes.

Generation of AAV8-Ap2.2-eGFP/Cre Virus. The AAV8-Ap2.2-eGFP/Cre virus was made by the University of Michigan Vector Core (Ann Arbor, MI, USA). In brief, the AP2.2 gene block was synthesized by IDT. The eGFP-Myc-Cre gene block was PCR amplified from the addgene plasmid #49056. The two fragments were assembled in a 3-part Gibson assembly into BstAPI/XhoI digested pCW3SL adeno-associated transfer plasmid (81) using NEB Gibson Assembly Master Mix following manufacturer's instructions and transformed into NEB

stable competent cells. Individual clones were picked and grown overnight before DNA miniprep. Assembly of the Ap2.2-eGFP/Cre plasmid was verified by Sanger sequencing. The Ap2.2-eGFP/Cre plasmid was then used to generate recombinant AAV8 virus by transfection of 293T cells and purified by iodixanol gradients. Titers of the viral preparations were determined by qPCR using a published protocol (https://www.addgene.org/protocols/aav-titration-qpcr-using-sybr-green-technology/).

Mice. All mice were housed at and cared for by the Unit for Laboratory Animal Medicine (ULAM) facilities at the University of Michigan and the Angeles Lab. Animals were housed in standardized conditions to avoid intergroup variation.

mT/mG indicator mice: B6.129(Cg)-*Gt(ROSA)26Sor*$^{tm4(ACTB\text{-}tdTomato,\text{-}EGFP)Luo}$/J mice (Jackson Laboratory, stock #007676) were used to assess the induction of the AAV8-Ap2.2-eGFP/Cre virus. Tissues were harvested 8 days post injection for staining.

Trp53$^{f/f}$*Pten*$^{f/f}$ *GEMM:* Trp53$^{f/f}$ mice (B6.129P2-*Trp53*^{tm1Brn}/J, Jackson Laboratory, stock #008462) were crossed with Pten$^{f/f}$ mice (B6.129S4-*Pten*^{tm1Hwu}/J, Jackson Laboratory, stock #006440) to produce homozygous *Trp53*$^{f/f}$ *Pten*$^{f/f}$ C57BL/6J mice. Genotyping was performed by TransnetYX (Cordova, TN).

Viral Injections. AAV8-Ap2.2-eGFP/Cre virus was diluted with PBS to a low (2.3×10^{10} vector genomes [vg]) and high dose (2.3×10^{11} vg) and injected subcutaneously into the left and right flank fat pads of mT/mG indicator mice to assess Cre-mediated recombination in the tissue. AAV8-Ap2.2-eGFP/Cre virus was diluted with PBS to concentrations ranging from 1.15×10^{10} vg to 1.62×10^{12} vg and injected subcutaneously into the left and right flank fat pads of *Trp53*$^{f/f}$*Pten*$^{f/f}$ mice or wild type C57BL/6J mice as control. Mice were anesthetized with 2.5% isoflurane for all virus injections.

Tumor monitoring and tissue harvesting. Tumor growth was monitored 3 times per week using digital calipers. Mice were euthanized and all tissues were harvested when a flank tumor reached 20 mm in diameter, as per University of Michigan Institutional Animal Care and Use Committee (IACUC) protocol. Tissues collected included tumors, spleens, lungs, liver and contralateral fat pad (when applicable). Fresh tissues were divided and stored in formalin fixed paraffin embedded (FFPE) blocks or in liquid nitrogen for future DNA and RNA extraction. Lungs, livers, and abdominal cavities were examined for macro-metastases at time of harvest. Lungs and livers were checked for microscopic disease via H&E. For virus-injected mice, if no tumors were observed 18 months following injection, mice were euthanized via CO_2 inhalation. For tail vein injections, mice were

euthanized for tissue collection if a tumor started to develop in an undesired location or 6 - 7 months post injection.

Magnetic Resonance Imaging (MRI) of ACPP mice. Mice injected with AAV8-Ap2.2-eGFP/Cre were imaged via MRI every 2 - 4 weeks following injection. Following anesthetization with 2% isoflurane, mice were laid prone, headfirst, in a horizontal bore 7.0T Bruker MR scanner with body temperature maintained at 37°C using circulating heated water. A quadrature volume radiofrequency coil was used to scan the abdominal region of mice. Gated coronal images were acquired using a T2-weighted rapid acquisition with relaxation enhancement (T2-TurboRARE) sequence with the following parameters: repetition time (TR)/effective echo time (TE), 3500/26 ms; echo spacing, 8.667 ms; number of echoes, 8; field of view (FOV), 40×50 mm; matrix, 256×128; slice thickness, 0.5 mm; number of slices, 40; and number of scans, 1.

Syngeneic cell line generation and culturing. Three cell lines (N1011, N1018, and N1343) were generated from three independent spontaneous ACPP DDLPS tumors (see Supplementary Figure 6C). In brief, 500 mg of tumor were rinsed with Hanks' Balanced Salt Solution (HBSS) and minced prior to digestion in collagenase IV solution [0.5 mg/mL DNAse (Sigma, 10104159001), 1 tablet Complete Mini EDTA-free Protease Inhibitor cocktail (Sigma, 11836170001), 5 mg/mL Collagenase Type IV (Sigma C5138-500mg)] for 30 minutes in a 37°C shaking incubator. Fetal bovine serum (FBS) was added to the suspension to stop the reaction. Samples were filtered through a 100 μM nylon mesh filter and pelleted via centrifugation at 450g and supernatant was discarded. Samples were resuspended in 1% FBS/PBS and filtered through a 40 μM nylon mesh filter. Samples were pelleted again as described above prior to being resuspended in growth media (GM) [DMEM HG F12 (Gibco 11320), 10% FBS, 100 U/mL Penicillin/Streptomycin, 2 mM L-glutamine and 2.5 ug/mL plasmoscin] and plated in a 6 well plate. Cells were cultured at 37°C in a humidified incubator with 5% CO_2 and were passaged when they approached confluency. Aliquots of cell lines were frozen down for storage at various passages (P3 – P7) in 10% DMSO/FBS.

Syngeneic cell line injections. For cell line-derived tumor formation, 250,000 – 1,000,000 tumor cells were suspended in growth media (GM) and mixed 1:1 in Matrigel (Fishers, 356231) to prepare 200 μL for subcutaneous injections. To assess metastatic potential, 100,000 tumor cells were resuspended in GM to prepare 100 μL injections. Cells were subcutaneously (flank) or intravenously (tail vein) injected into 8 – 12-

week-old WT C57BL/6J mice (Jackson Laboratory, stock #000664). Mice were anesthetized with 2.5% isoflurane for all cell injections.

3T3 cell line differentiation and culturing. CL-173 3T3-L1 (3T3) cells were purchased from ATCC (Lot #70043674). Cells were expanded using expansion cell media [DMEM (11965-084) with 10% CALF serum (ATCC 30-2030), 100 U/mL Penicillin/Streptomycin, 2 mM L-glutamine and 2.5 ug/mL plasmoscin]. Cells were cultured at 37°C in a humidified incubator with 10% CO_2. Cells were passaged and expanded when they approached confluency. Cells were differentiated using differentiation media [DMEM (11965-084) with 10% FBS, 100 U/mL Penicillin/Streptomycin, 250 mM IBMX (Sigma, I5879-250mg), 10 mg/mL insulin (Sigma, I0516-5mL), 10 mM Dexamethasone (Sigma, D4902-25mg), 25 mM Rosiglitazone (Sigma, R2408-10mg)] on days 1-3. Next, cells were cultured in high insulin media [DMEM (11965-084) with 10% FBS, 100 U/mL Penicillin/Streptomycin, 10 mg/mL insulin (Sigma, I0516-5mL)] on days 4-6. Media was replaced with expansion cell media on days 7-9 for final differentiation to lipid producing adipocytes.

Immunohistochemistry (IHC). Tissues were fixed for 24 hours in 10% neutral-buffered formalin and transferred to 70% ethanol before being embedded in paraffin and sectioned. Hematoxylin (Leica, Surgipath, Cat #3801562) and eosin (Leica, Surgipath, Cat #3801601) (H&E) stain and desmin were performed on FFPE sectioned mouse tissues following standard protocol by the University of Michigan Rogel Cancer Center Histology Core on the Ventana Discovery Ultra (Roche, Indianapolis, Indiana, USA). See Supplementary Table 3 for antibody details. DAPI (Abcam, AB228549) was used to stain nuclei. mT/mG indicator mice samples were stained for GFP and tdTomato using the ABC method (82) to assess Cre-mediated recombination in adipocytes/fat pads and distant organs.

Histopathological analysis. Histopathologic categorization was performed and independently categorized by two soft tissue pathologists using commonly accepted morphologic criteria for human WD/DDLPS. Diagnostic features of WDLPS included fibrous septa containing atypical mesenchymal cells with enlarged, irregular or hyperchromatic nuclei in the background of adipocytes. Typical identifying features of DDLPS included abrupt loss of adipocytic morphology, in which the tumor was composed of sheets of pleomorphic or highly atypical, spindled cells. During microscopic examination, the amount of tumor infiltrating lymphocytes (TIL) was also approximated. Tumors with occasional lymphocytes in contact with tumor cells over ten fields of high magnification (400×) were designated low TIL and those with lymphocytes consistently in contact with tumor

cells at medium magnification (200×) were designated moderate TIL. In high TIL tumors, lymphocytes were easily apparent at low magnification (100×) and at least focally obscured by clusters of sarcoma cells.

Spectral Flow Cytometry Sample Preparation. Cell line-derived tumor samples were minced and digested in RPMI (cat#) containing 2 mg/mL collagenase Type IV (Sigma, C5138-500mg) and 1 mg/mL DNase I (Sigma, 10104159001) at 37°C for 30 minutes. Dissociated cells were filtered through a 70 μM nylon mesh filter and washed with FACS buffer. Cells were then stained with the viability dye FVS780 for 30 minutes at 4°C. Upon removing the viability stain, Fc receptors were blocked with anti-mouse FC blocking Ab (Bio X Cell). Cells were then incubated for 45 minutes at 4°C for surface marker targets listed in Supplementary Table 2. Cells were washed with Flow buffer, fixed with Fixation Medium A for 15 minutes at room temperature and then strained through a 35 μM filter cap tube and stored overnight at 4°C. Flow cytometry data were collected and compensated via unmixing on the Cytek Aurora at the University of Michigan Flow Cytometry Core (Ann Arbor, Michigan, USA) and data were analyzed using FlowJo™ v10 software (BD Life Sciences).

Spectral Flow Cytometric Analysis. Unmixed FCS files were analyzed using traditional gating methods for lymphocytes (Supplementary Figure 7B) and myeloid populations (Supplementary Figure 7C). Three cell line-derived tumor samples containing median levels of CD3+ T cells as determined via manual gating for each respective cell line were selected for dimensionality reduction analysis via t-distributed Stochastic Neighbor Embedding (t-SNE) using FlowJo™ v10 software (BD Life Sciences). Samples were pre-gated using the gating strategy in Supplemental Figure 7A and down sampled to 15K events per sample using DownSample v3.3.1. FCS files for each sample were concatenated prior to running t-SNE using the following settings: opt-SNE learning configurations at 1000 iterations, 30 perplexity, the random projection forest KNN algorithm, and the Barnes-Hut gradient algorithm (83, 84). Clustering was performed via FlowSOM v4.1.0. Multiple iterations were performed to determine the optimal number of clusters (16 populations were selected). Only clusters with > 500 cells were considered (n = 1 cluster excluded from analysis). The generated meta-cluster heatmap was used to name the clusters (Supplemental Figure 9A).

Multiplex fluorescent immunohistochemistry (mIHC) staining and imaging. 5 μm paraffin-embedded tissue slices were placed onto charged slides, baked for 1 hour at 60°C, rehydrated as prior, and fixed with formalin. Multiplex staining was conducted as previously described (44) utilizing the OPAL platform and 6-plex manual detection kit (Akoya, #NEL861001KT). Briefly, slides were prepared for each round of staining using

either an antigen retrieval buffer with pH 9 or pH 6 (AR9 and AR6, Akoya Biosciences), followed by antibody application (Standard Immune Panel - $CD3^+$ (Opal 520), $CD8\alpha^+$ (Opal 570), $FOXP3^+$ (Opal 780), $PD\text{-}1^+$ (Opal 690), $F4/80^+$ (Opal 480), $CD19^+$ (Opal 620); T_{RM} Panel: $CD3^+$ (Opal 480), $CD8\alpha^+$ (Opal 520), $CD103^+$ (Opal 570), $CD69^+$ (Opal 620), and $PD\text{-}1^+$ (Opal 690)), secondary antibody application, and fluorescent tyramide signal amplification. Slides were counterstained with 4'6-diamidino-2-phenylindole (DAPI) and a composite image obtained on the Vectra Polaris microscope. Ten regions of interest were identified for each tumor or slide, and using InForm software (Akoya Biosciences), each individual cell was assigned a cellular phenotype and unique spatial location, allowing for quantification of proportion of tumor-associated immune cell subtypes, inter-cellular distances, and nearest neighbor calculations as previously described (44).

*DNA and RNA Extraction***.** Tissue samples were stored in liquid nitrogen or RNAlater stabilization solution until extraction. 30 mg of frozen tissue was dissociated using the BeadBug Homogenizer (Southern Labware, D1030). DNA and RNA was extracted using the AllPrep DNA/RNA Mini Kit (Qiagen 80204). DNA and RNA concentrations were determined using the NanoDrop 2000 (Thermo Fisher Scientific)

Quantitative reverse transcription PCR. Samples were stored either in liquid nitrogen or RNAlater and were dissociated using the BeadBug Homogenizer (Southern Labware, D1030). RNA was extracted using the RNeasy Mini Kit (Qiagen #74104). RNA was quantified using the NanoDrop 2000 and 200 ng was used for reverse transcription with the High-Capacity cDNA RT kit (Applied Biosystems #4368814). Cycle was 25°C 10 minutes, 37°C 2 hours, 85°C 5 minutes. qPCR was performed using Fast SYBR Green Master Mix (Thermo Fisher Scientific). Primers are listed in Supplemental Table 3. RNA levels were normalized to GAPDH RNA levels using the $2^{-\Delta Ct}$ method.

Whole Exome Sequencing (WES). Whole exome sequencing was performed on genomic DNA from murine ACPP tumors (n = 14) on an Illumina NovaSeq 6000 by Novogene. Sample preparation, sample QC, library preparation, library QC, sequencing, and data QC were performed by Novogene. Exome enrichment was performed using Agilent SureSelectXT Mouse Exon Kit and 150 bp paired-end reads were generated with sequencing depth above 50X (6G).

Whole Exome Sequencing (WES) Analysis. Samples were aligned to mm39 using Burrows-Wheeler aligner (BWA). We used "CNVKit" for copy number variation analysis. We used "KaryoploteR" R package for visualizing coverage and log ratio. The log ratio for *Trp53* and *Pten* exon 5 was calculated using a weighted

average of CNVKit bin-level calls of bins overlapping gene regions. The fraction of genome altered (FGA) was determined by dividing the total length of altered segments by the mouse genome size (~2.7 Gb).

Bulk RNA sequencing. Messenger RNA was purified from total RNA using poly-T oligo-attached magnetic beads. After fragmentation, first strand cDNA was synthesized using random hexamer primers, followed by the second strand cDNA synthesis using dUTP for directional library or dTTP for non-directional library. The library was checked with Qubit and real-time PCR for quantification and bioanalyzer for size distribution detection. Quantified libraries were pooled and sequenced on Illumina platforms based on effective library concentration and data amount. Index-coded samples were clustered according to the manufacturer's instructions. After cluster generation, library preparations were sequenced on an Illumina platform and paired-end reads were generated. Raw reads in fastq format were processed through fastp software. Clean reads were obtained by removing low-quality reads and reads containing adapters and ploy-N from raw data. At the same time, Q20, Q30 and GC content within clean data were calculated. All downstream analyses were based on clean data. Reference genome (GRCm39) and gene model annotation files were downloaded from the genome website. The index of the reference genome was built using Hisat2 v2.0.5 and paired-end clean reads were aligned to the reference genome using Hisat2 v2.0.5. featureCounts v1.5.0-p3 was used to count the read numbers mapped to each gene. Fragments per kilobase of transcript (FPKM) of each gene was calculated based on the length of the gene and reads count mapped to this gene. Sequencing was performed by both Novogene and the Advanced Genomics Core at the University of Michigan.

Bioinformatics Analysis. Mean tumor volume (mm^3) analysis and visualization was performed using GraphPad Prism 10 (GraphPad Software, Inc). WES analysis was performed using the Python library CNVKit to detect copy number variants and alterations genome-wide from high-throughput sequencing data. Spectral flow cytometric and mIHC quantification data and FGA data were visualized using "ggplot2" to create boxplots and barplots and "pheatmap" to make heatmaps; "ggpubr" was utilized to determine statistical significance between groups and "BayesFactor" was utilized to determine statistical significance between proportion composition among groups. Count data from RNA sequencing was analyzed using DESeq2. Variance stabilizing transformation (vst()) function was used to generate normalized count matrix for visualization. PCAtools R packages were used to generate PCA plots. Differentially expressed genes between WDLPS vs. normal fat and DDLPS vs. normal fat were defined using DESeq() function with 'condition' and 'batch' as covariates. Gene Set

Enrichment Analysis (GSEA) was done using the fgsea R package using the MSigDB Hallmarks (MH) gene set, which was download using msigdb R package. GSEA was used to score enrichment of gene sets differentially expressed human in WDLPS vs normal fat and DDLPS vs normal fat in mouse RNAseq comparisons. The convert_human_to_mouse_symbols() function from nichenetR R package was used to convert human genes to mouse homologs. Gene Set Variation Analysis (GSVA) (85) was utilized to score for the cell-type signatures defined by murine Microenvironment Cell Population counter (mMCP) (47). Heatmaps visualizing expression were generated using “ggplot2” and “pheatmap” R packages. Volcano Plots visualizing differential gene expression, calculated using DESeq() and lfcShrink(), were created using the “EnhancedVolcano” R package.

Human sample collection. All human studies were performed in accordance with ethical regulations and pre-approved by the University of Michigan Medical School Institutional Review Board (IRBMED) (#HUM00196054). Patients with soft tissue tumors provided written informed consent to obtain fresh tissue from surgical specimens as part of the Sarcoma Research Working Group Biobank at the University of Michigan Rogel Cancer Center. Samples were obtained from patients who had a pathological diagnosis of liposarcoma.

Study Approval. All animal studies were reviewed and approved by the University of Michigan Institutional Animal Care and Use Committee (IACUC) under animal protocol #PRO00011576. All animals were housed, maintained, and handled according to the guidelines at the University of Michigan, which is accredited by the American Association for the Assessment and Accreditation of Laboratory Animal Care (AALAC). All animal experiments complied with AALAC guidelines, US Department of Health and Human Services policies, and local and federal laws regarding animal welfare.

Statistics. Significance was evaluated by the following statistical analyses: student’s t-test for 2 groups, non-parametric Wilcoxon Rank Sum (Mann-Whitney) or Kruskal-Wallis for 3 or more groups, or Chi-square test for proportion comparison. Specific tests are denoted in the figure legends. Analyses were made in R using ggplot2 (3.5.1) and ggpubr (0.6.0) using the stat_compare_means() and stat_summary() functions. P values were adjusted for multiple comparisons with the Bonferroni correction method when appropriate. Data are presented as means ± standard error (SEM) or means ± standard deviation (STDV). Individual data points are shown, or n is indicated. A P value cut-off of $P < 0.05$ was considered statistically significant.

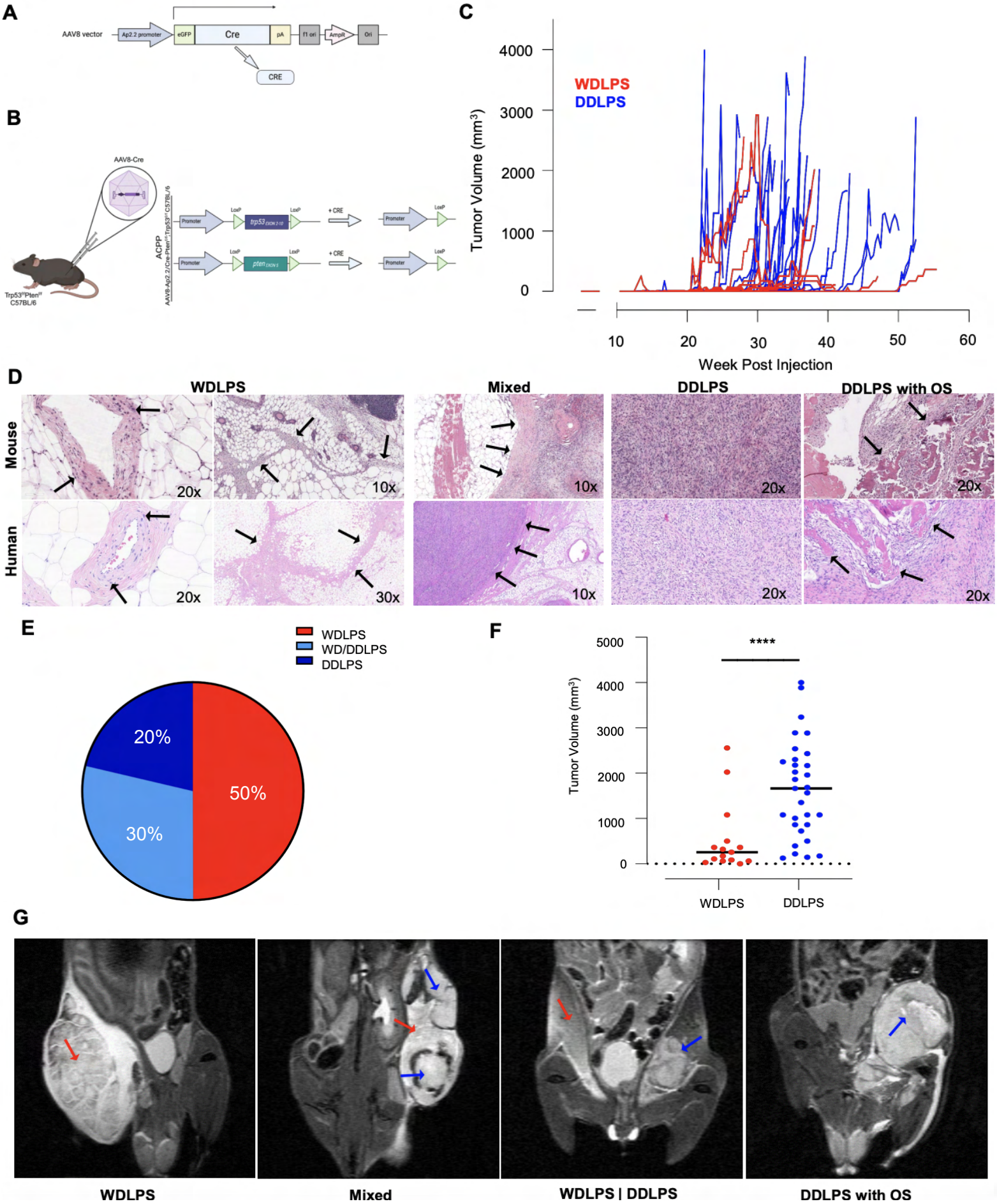
A
AAV8 vector
Ap2.2 promoter
eGFP
Cre
pA
f1 ori
AmpR
Ori
CRE
B
AAV8-Cre
ACPP
Promoter
LoxP
+ CRE
C
WDLPS
DDLPS
Tumor Volume (mm³)
Week Post Injection
D
WDLPS
Mixed
DDLPS
DDLPS with OS
Mouse
Human
20x
10x
30x
E
WDLPS
WD/DDLPS
DDLPS
50%
30%
20%
F
****
Tumor Volume (mm³)
WDLPS
DDLPS
G
WDLPS
Mixed
WDLPS | DDLPS
DDLPS with OS

Figure 1

Figure 1. Targeted deletion of *Trp53* and *Pten* in ACPP model generates murine LPS histologically similar to human LPS. (**A**) Creation of an adipocyte-specific promoter sequence to drive an eGFP-Myc tag-Cre fusion molecule. (**B**) Schematic of orthotopic injection of AAV8-Ap2.2-eGFP/Cre into *Trp53*$^{f/f}$*Pten*$^{f/f}$ C57BL/6 GEMM which generates LPS tumors. (**C**) Tumor volume (mm^3) growth curves in weeks post injectin of AAV8-Ap2.2-eGFP/Cre injection for WDLPS (red; n = 15) and DDLPS (blue; n = 31). (**D**) H&E of spontaneous ACPP WDLPS, mixed WDLPS/DDLPS, and DDLPS (top row) show similar histological changes as human subtype specific LPS (bottom row). From left to right features of both murine and human tumors: WDLPS: atypical cells (arrows) entrapping vessels, WDLPS: fibrous septa (arrows) containing cells with atypical nuclei, Mixed: stark transition (arrows) between WDLPS and DDLPS components, DDLPS: consisting of atypical spindled and pleomorphic cells that exhibit a storiform to vaguely fascicular architecture, and DDLPS: containing areas of bone formation (arrows), compatible with heterologous OS differentiation. (**E**) Histology distributions of spontaneous ACPP LPS tumors. Red = WDLPS; Light Blue = mixed WDLPS/DDLPS; Dark Blue = DDLPS. (**F**) Tumor volume (mm^3) of WDLPS (red) and DDLPS (blue). Mean tumor volume is shown. Statistical differences determined by student's t-test. Significance is indicated by **** = $P < 0.0001$. (**G**) MRI images of mouse LPS tumors, from left to right: WDLPS on the right flank (far left), WDLPS transitioning into DDLPS on the left flank (left), WDLPS on right flank and DDLPS on left flank (right), and DDLPS with heterologous OS differentiation on the left flank (far right). Red arrows: WDLPS; blue arrows: DDLPS. Panels 1A and 1B created in BioRender.

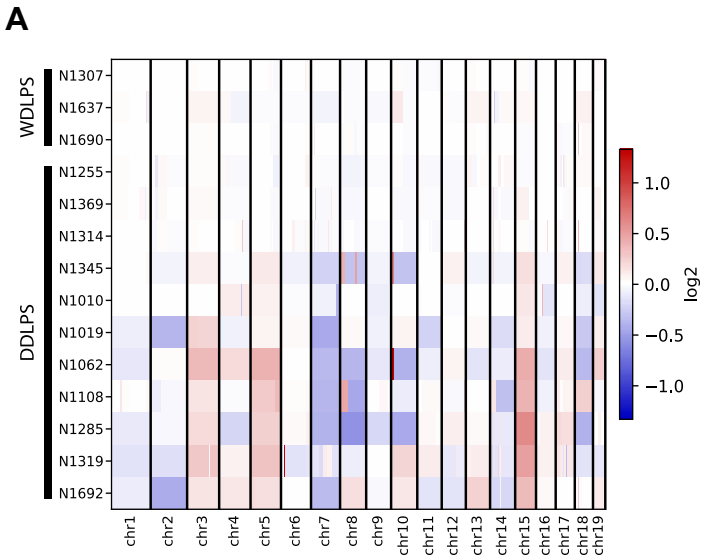

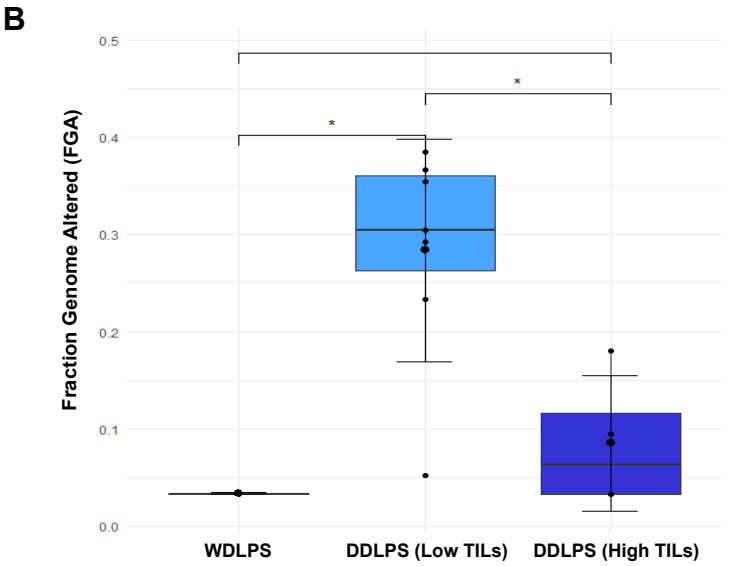

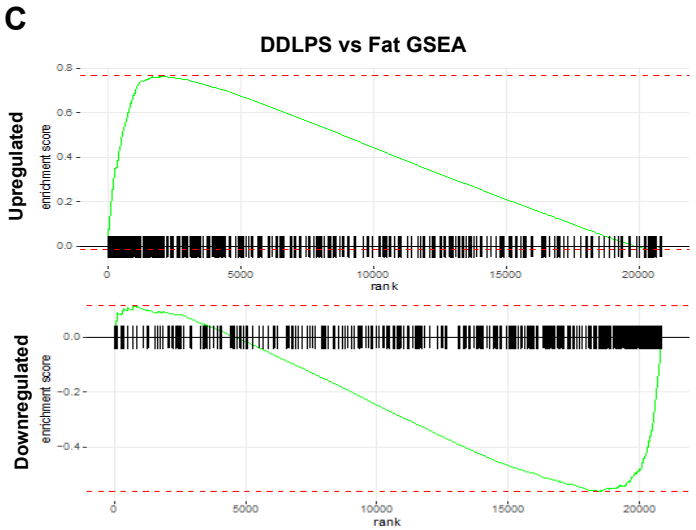

D

	Mouse		Human	
Hallmark Pathway	**NES**	**P adj**	**NES**	**P adj**
G2M Checkpoint	2.21	1.2e-13	2.80	2.5e-23
E2F Targets	2.29	1.6e-16	2.70	1.4e-21
Epithelial Mesenchymal Transition	2.40	1.0e-21	2.37	5.5e-12
Adipogenesis	-3.04	7.7e-33	-3.28	2.8e-39
Fatty Acid Metabolism	-2.05	1.2e-7	-2.88	3.2e-19
Oxidative Phosphorylation	-2.68	2.2e-19	-3.15	2.3e-32

Figure 2

Figure 2. Murine ACPP tumors transcriptomically resemble human LPS. (**A**) Heatmap of segmented log2-ratio read coverage comparing 14 spontaneous murine ACPP tumors to normal fat using whole exome sequencing (WES) data, as analyzed by CNVkit. The heatmap represents genome-wide copy number alterations grouped by histological classification. Red blocks indicate chromosomal region gains, while blue blocks indicate chromosomal region losses. (**B**) Boxplot depicting the Fraction of Genome Altered (FGA) across distinct histologies (WDLPS $n = 3$, DDLPS (Low TILs) $n = 7$, DDLPS (High TILs) $n = 4$). Statistical differences determined by non-parametric Wilcoxon Rank Sum (Mann-Whitney) test. Significance is indicated by * = $P < 0.05$; ** = $P < 0.01$. (**C**) Gene set enrichment analysis (GSEA) of upregulated and downregulated gene sets in mouse ACPP DDLPS ($n = 10$) compared human DDLPS ($n = 8$) (relative to species specific normal fat, mouse $n = 4$; human $n = 8$) show concordance (NES 2.5, padj $2x10^{-50}$ and 2.5, $9.5x10^{-35}$, respectively). (**D**) Hallmark Pathways that are significantly up- or downregulated in both murine ACPP and human DDLPS in comparison to species-specific normal fat.

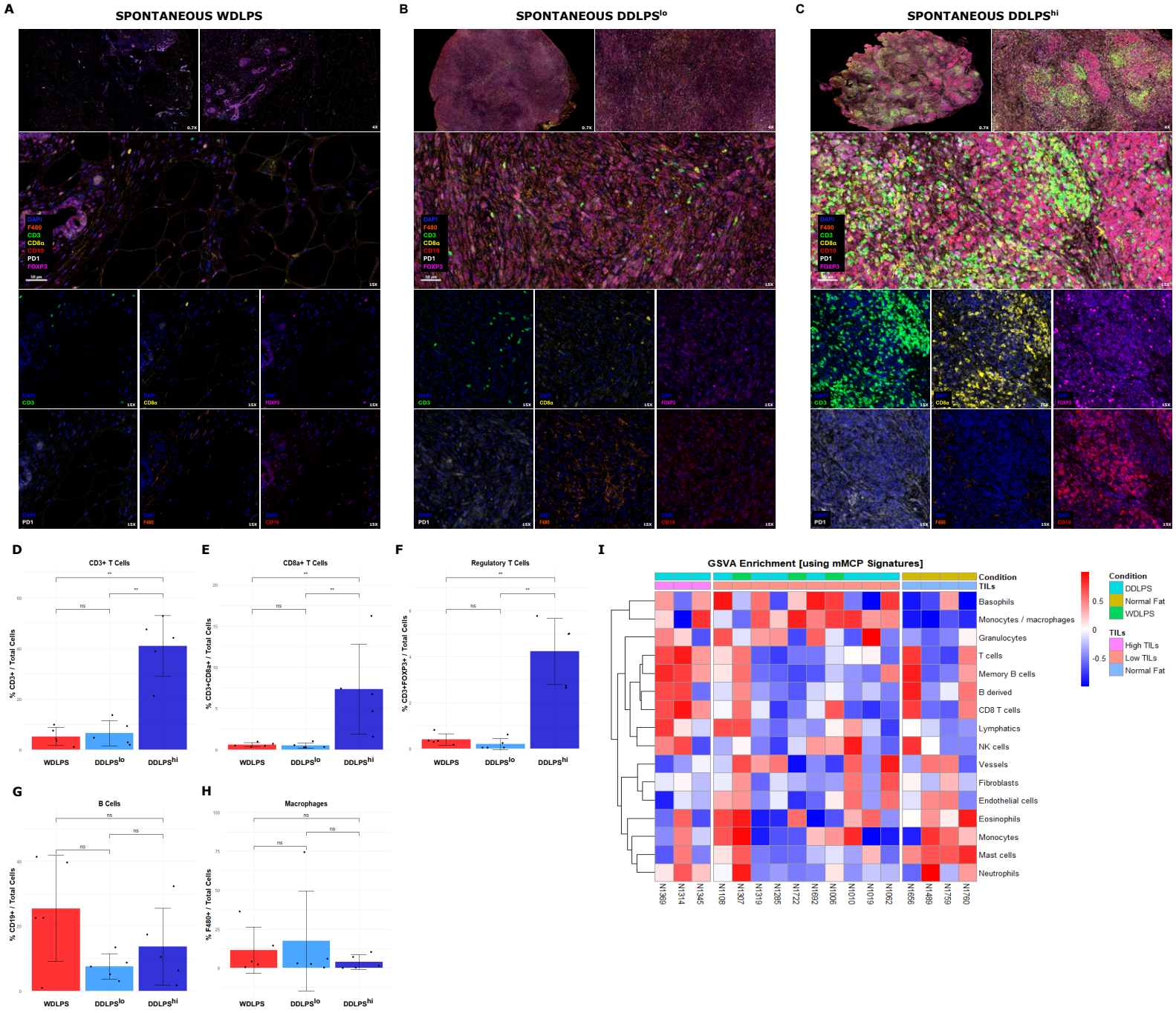
A
SPONTANEOUS WDLPS
B
SPONTANEOUS DDLPS^{lo}
C
SPONTANEOUS DDLPS^{hi}
DAPI
F480
CD3
CD8a
CD19
PD1
FOXP3
D
CD3+ T Cells
% CD3+ / Total Cells
E
CD8a+ T Cells
% CD3+CD8a+ / Total Cells
F
Regulatory T Cells
% CD3+FOXP3+ / Total Cells
G
B Cells
% CD19+ / Total Cells
H
Macrophages
% F480+ / Total Cells
WDLPS
DDLPS^{lo}
DDLPS^{hi}
ns
I
GSVA Enrichment [using mMCP Signatures]
Condition
TILs
Basophils
Monocytes / macrophages
Granulocytes
T cells
Memory B cells
B derived
CD8 T cells
Lymphatics
NK cells
Vessels
Fibroblasts
Endothelial cells
Eosinophils
Monocytes
Mast cells
Neutrophils
N1369
N1314
N1345
N1108
N1307
N1319
N1285
N1722
N1692
N1006
N1010
N1019
N1062
N1656
N1489
N1759
N1760
0.5
0
-0.5
DDLPS
Normal Fat
WDLPS
High TILs
Low TILs
Normal Fat

Figure 3

Figure 3. Spontaneous ACPP tumors have distinct TIMEs defined by variations in T cell population density. (**A-C**) Multiplex IHC (mIHC) of spontaneous ACPP tumors representing WDLPS (**A**) and DDLPS with low (**B**) or high TILs (**C**). mIHC standard immune panel comprised of stains for $CD3^+$ (green), $CD8\alpha^+$ (yellow), $FOXP3^+$ (magenta), $PD\text{-}1^+$ (white), $F4/80^+$ (orange), and $CD19^+$ (red) with DAPI nuclear stain (Hoechst/blue). Shown at 0.7X, 4X, and 15X magnifications. Scale bar as shown. (**D-I**) Quantification of mIHC via inForm analysis for $CD3^+$ (**D**), $CD3^+CD8\alpha^+$ (**E**), $CD3^+FOXP3^+$ (**F**), $CD19^+$ (**G**), and $F480^+$ (**H**) positive cells. $DDLPS^{lo}$ defined as samples with < 20% total $CD3^+$ positive cells and $DDLPS^{hi}$ defined as samples with > 20% $CD3^+$ positive cells out of total cells (# of nuclei). Data, mean ± SEM; n = 5 samples/histology subclassification. Statistical differences determined by non-parametric Wilcoxon Rank Sum (Mann-Whitney) test. Significance is indicated by * = $P < 0.05$; ** = $P < 0.01$. (**I**) Heatmap plot representing the value of the GSVA enrichment score, using mMCP gene signatures for immune cells, calculated for normal fat (n = 4) and ACPP tumor (n = 13) samples; grouped by H&E TILs classification.

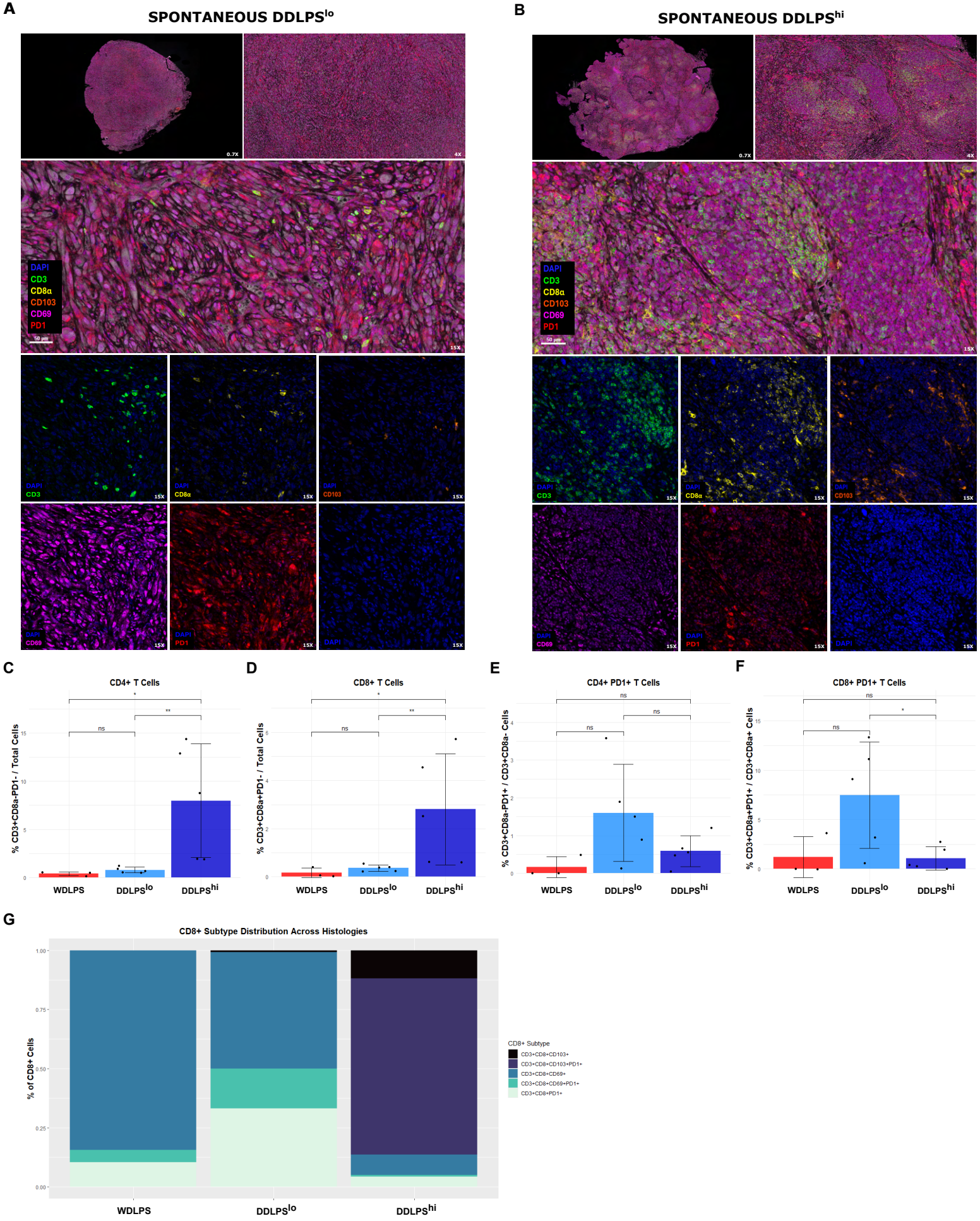
A
SPONTANEOUS DDLPS^{lo}
B
SPONTANEOUS DDLPS^{hi}
DAPI
CD3
CD8α
CD103
CD69
PD1
C
CD4+ T Cells
% CD3+CD8a-PD1- / Total Cells
D
CD8+ T Cells
% CD3+CD8a+PD1- / Total Cells
E
CD4+ PD1+ T Cells
% CD3+CD8a-PD1+ / CD3+CD8a- Cells
F
CD8+ PD1+ T Cells
% CD3+CD8a+PD1+ / CD3+CD8a+ Cells
ns
WDLPS
DDLPS^{lo}
DDLPS^{hi}
G
CD8+ Subtype Distribution Across Histologies
% of CD8+ Cells
CD8+ Subtype
CD3+CD8+CD103+
CD3+CD8+CD103+PD1+
CD3+CD8+CD69+
CD3+CD8+CD69+PD1+
CD3+CD8+PD1+

Figure 4

Figure 4. CD8+ T cell phenotypes vary significantly between DDLPS^{lo} and DDLPS^{hi} tumors . (**A-B**) Multiplex IHC (mIHC) of spontaneous ACPP tumors representing DDLPS with low (**A**) or high T cells (**B**). mIHC resident memory T cell (T_{RM}) panel comprised of stains for CD3$^+$ (green), CD8α$^+$ (yellow), CD103$^+$ (orange), CD69$^+$ (magenta), and PD-1$^+$ (red) with DAPI nuclear stain (Hoechst/blue). Shown at 0.7X, 4X, and 15X magnifications. Scale bar as shown. (**C-F**) Quantification of mIHC via inForm analysis for CD3$^+$CD8α$^-$PD1$^-$ (**C**), CD3$^+$CD8α$^+$PD1$^-$ (**D**), CD3$^+$CD8α$^-$PD1$^+$ (**E**), and CD3$^+$CD8α$^+$PD1$^+$ (**F**) positive cells. DDLPS^{lo} defined as samples with < 20% total CD3$^+$ positive cells and DDLPS^{hi} defined as samples with > 20% CD3$^+$ positive cells. Data, mean ± SEM; n = 5 for DDLPS^{lo} and DDLPS^{hi} samples and n = 3 for WDLPS samples. Statistical differences determined by non-parametric Wilcoxon Rank Sum (Mann-Whitney) test. Significance is indicated by * = P < 0.05; ** = P < 0.01. (**G**) Stacked bar graph of the proportion of CD8α$^+$ phenotypes in ACPP tumors (n = 13) stratified by histological subclassifications; each phenotype is represented as a percentage of the whole; phenotypes whose percentage of the whole was 0 are not shown. Statistical difference in proportion composition determined by non-parametric Chi-square (X^2) test.

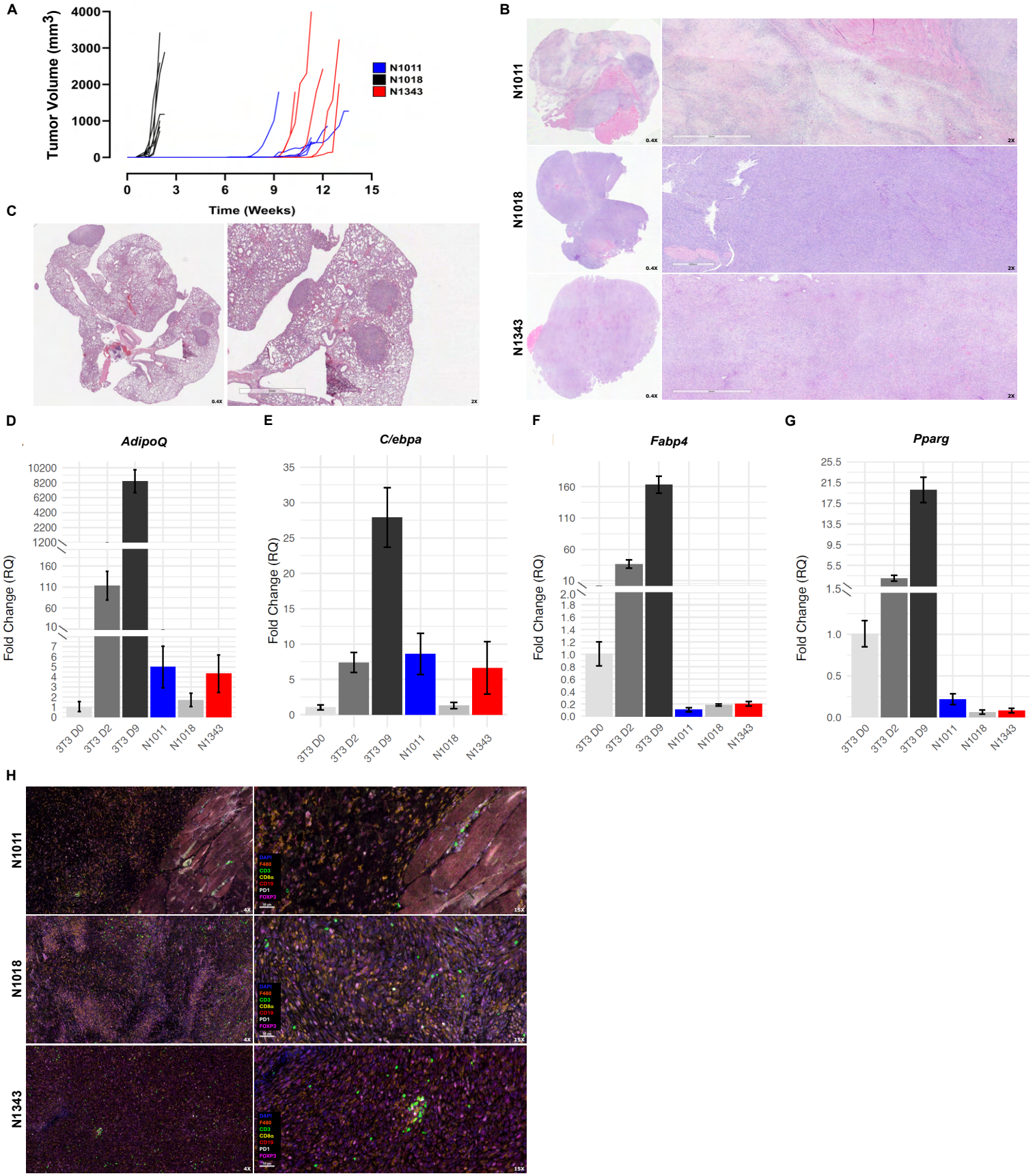
A
Tumor Volume (mm3)
4000
3000
2000
1000
0
0
3
6
9
12
15
Time (Weeks)
N1011
N1018
N1343
B
N1011
N1018
N1343
C
D
AdipoQ
Fold Change (RQ)
3T3 D0
3T3 D2
3T3 D9
N1011
N1018
N1343
E
C/ebpa
Fold Change (RQ)
F
Fabp4
Fold Change (RQ)
G
Pparg
Fold Change (RQ)
H
N1011
N1018
N1343
DAPI
F480
CD3
CD8a
CD19
PD1
FOXP3

Figure 5

Figure 5. Syngeneic cell lines derived from spontaneous ACPP tumors develop orthotopic DDLPS tumors and lung metastases in WT C57BL/6 mice. (**A**) Tumor growth curves, represented by tumor volume (mm^3), shown in weeks following cell line injection for N1011 (blue; *n* = 5), N1018 (black; *n* = 7) and N1343 (red; *n* = 5). (**B**) Representative H&Es of CLDTs N1011, N1018, and N1343 at 0.4X (left) and 2X (right) magnification. Scale bar as shown. (**C**) Representative H&E of N1018 tail vein injected metastases in the lung at 0.4X (left) and 2X (right) magnification. Scale bar shown. (**D-G**) Analysis of gene expression levels in pre-adipocytes (3T3 day 0 =D0), adipocytes treated with differentiation factors for early differentiation (3T3 day 2=D2) and late differentiation/mature adipocytes (3T3 day 9=D9), and each cell line for mature adipocyte markers *AdipoQ* (**D**), *C/ebpa* (**E**), *Fabp4* (**F**), or *Pparg* (**G**). Gene expression was quantified using qRT-PCR and normalized to *Gapdh*. Samples were analyzed in triplicates. Data are presented as relative fold change (RQ) calculated by the 2A(-MCt) method. (**H**) Representative mIHC of CLDTs (N1011 and N1018 *n* = 3, N1343 *n* = 2) stained with immune cell markers $CD3^+$ (green), $CD8\alpha^+$ (yellow), $FOXP3^+$ (magenta), $PD\text{-}1^+$ (white), $F480^+$ (orange), and $CD19^+$ (red) with DAPI nuclear counterstain (Hoechst/blue). Shown at 4X (left) and 15X (right) magnification. Scale bar shown.

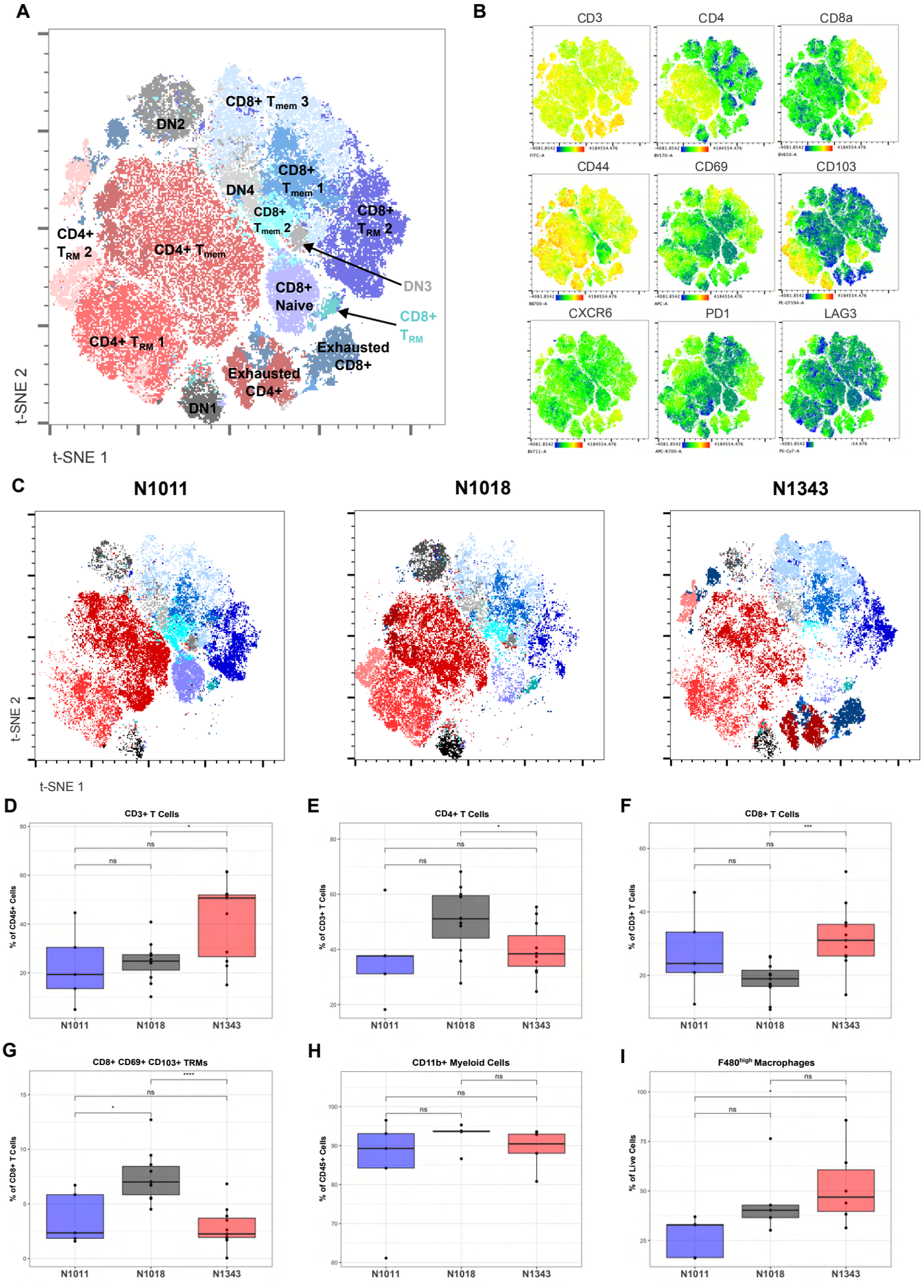
A
CD8+ Tmem 3
DN2
CD8+ Tmem 1
DN4
CD8+ Tmem 2
CD8+ TRM 2
CD4+ TRM 2
CD4+ Tmem
DN3
CD8+ Naive
CD8+ TRM
CD4+ TRM 1
Exhausted CD8+
Exhausted CD4+
DN1
t-SNE 2
t-SNE 1
B
CD3
CD4
CD8a
CD44
CD69
CD103
CXCR6
PD1
LAG3
C
N1011
N1018
N1343
t-SNE 2
t-SNE 1
D
CD3+ T Cells
% of CD45+ Cells
E
CD4+ T Cells
% of CD3+ T Cells
F
CD8+ T Cells
% of CD3+ T Cells
G
CD8+ CD69+ CD103+ TRMs
% of CD8+ T Cells
H
CD11b+ Myeloid Cells
% of CD45+ Cells
I
F480high Macrophages
% of Live Cells
N1011
N1018
N1343
ns

Figure 6

Figure 6. Orthotopic DDLPS cell-line derived tumors have variable TIL profiles. (**A**) t-SNE map generated using FlowJo from merged, pre-gated $CD3^+$ cells from N1011, N1018, and N1343 samples *(n* = 3 / cell line) from spectral flow cytometry. (**B**) Heatmaps of markers mean fluorescent intensity (MFI) overlayed on t-SNE map of all samples. MFI scale bar and fluorophores for each marker are shown. (**C**) t-SNE maps showing samples split by cell line highlighting differences in clusters between cell lines. (**D-G**) Lymphocyte populations between CLDTs analyzed via spectral flow cytometry and manually pre-gated on lymphocytes/singlets/live/$CD45^+$ (*n* = 5 – 10 per cell line) (**H-I**) Myeloid populations between CLDTs analyzed via spectral flow cytometry and manually pre-gated on all cells/singlets/live/$CD45^+$ (*n* = 5 - 10 per cell line; see gating strategy in Supplemental Figure 8C). In (**D-I**), the box plots represent mean (center line), the length of the box represents the 25th to 75th percentiles and the whiskers represent the 5th to 95th percentiles of the data. Outliers are shown as dots outside of whiskers. P values were calculated by the Kruskal-Wallis test. Significance is indicated by * = $P < 0.05$; *** = $P < 0.001$; **** = $P < 0.0001$. Flow cytometry gating strategy, see Supplemental Figure 8, A and B.

Author contributions

CVA conceptualized the study, designed the experiments, interpreted the data, wrote and finalized the manuscript, and supervised the project. AMS, EK, and LFG performed experiments, analyzed and interpreted the data, and wrote and finalized the manuscript. AME and MKI performed bioinformatics analyses and finalized the manuscript. KDP and SCB performed the pathological analysis, interpreted the data, provided relevant advice, and finalized the manuscript. JW, WY, BK, JM, JMD, and CEE conducted experiments. CJG analyzed MRI images. WJ assisted with the initial experimental design. AHC interpreted data and provided relevant advice. RC, TLF, MPM and AAD provided key materials, interpreted data and provided relevant advice. The order in which the co-first authors are listed was determined by the order of their entry into the study. All authors reviewed the manuscript.

Acknowledgments

The authors thank our pathology technician, Deb Postiff, for her dedication and time procuring human tumors. We thank Drs. Ormond MacDougald and Kenneth Lewis for support and guidance with adipocyte molecular biology techniques and confocal microscopy. We thank Lee Olsen for assistance with editing the manuscript. This work was supported by the National Cancer Institute (NCI) of NIH (R03 CA280126 to CVA; NCI Cancer Center Support Grant P30 CA046592 to CVA, T32 GM141840 to LFG) and a Rogel Cancer Center Discovery Grant to CVA. EK is supported by the University of Michigan Doctoral Program in Cancer Biology. We thank the Rogel Cancer Center Tissue and Molecular Pathology, Flow Cytometry, Single Cell and Spatial Analysis, and Preclinical Molecular Imaging Shared Resources, which are supported by NCI under P30 CA046592; the Vector Core at the University of Michigan Medical School; the Advanced Genomics Core at the University of Michigan, supported by NCI under P30 CA046592, where library prep and next-generation sequencing was completed; and the Unit for Laboratory Animal Medicine of the University of Michigan Medical School Office of Research. The authors thank the sarcoma patients whose tissue donations make this impactful research possible.

REFERENCES

1. Bredbeck BC, Delaney LD, Kathawate VG, Harter CA, Wilkowski J, Chugh R, et al. Factors associated with disease-free and abdominal recurrence-free survival in abdominopelvic and retroperitoneal sarcomas. *J Surg Oncol*. 2022;125(8):1292-300.
2. Singer S, Antonescu CR, Riedel E, and Brennan MF. Histologic subtype and margin of resection predict pattern of recurrence and survival for retroperitoneal liposarcoma. *Ann Surg*. 2003;238(3):358-70; discussion 70-1.
3. Keung EZ, Ikoma N, Benjamin R, Wang WL, Lazar AJ, and Feig BW. The clinical behavior of well differentiated liposarcoma can be extremely variable: A retrospective cohort study at a major sarcoma center. *J Surg Oncol*. 2018;117(8):1799-805.
4. Bock S, Hoffmann DG, Jiang Y, Chen H, and Il'yasova D. Increasing Incidence of Liposarcoma: A Population-Based Study of National Surveillance Databases, 2001-2016. *Int J Environ Res Public Health*. 2020;17(8).
5. Dalal KM, Antonescu CR, and Singer S. Diagnosis and management of lipomatous tumors. *J Surg Oncol*. 2008;97(4):298-313.
6. Demetri GD, von Mehren M, Jones RL, Hensley ML, Schuetze SM, Staddon A, et al. Efficacy and Safety of Trabectedin or Dacarbazine for Metastatic Liposarcoma or Leiomyosarcoma After Failure of Conventional Chemotherapy: Results of a Phase III Randomized Multicenter Clinical Trial. *J Clin Oncol*. 2016;34(8):786-93.
7. Benjamin RS, Baker LH, O'Bryan RM, Moon TE, and Gottlieb JA. Advances in the chemotherapy of soft tissue sarcomas. *Med Clin North Am*. 1977;61(5):1039-43.
8. von Mehren M, Kane JM, Agulnik M, Bui MM, Carr-Ascher J, Choy E, et al. Soft Tissue Sarcoma, Version 2.2022, NCCN Clinical Practice Guidelines in Oncology. *J Natl Compr Canc Netw*. 2022;20(7):815-33.
9. Somaiah N, and Tap W. MDM2-p53 in liposarcoma: The need for targeted therapies with novel mechanisms of action. *Cancer Treat Rev*. 2024;122:102668.
10. Cornillie J, Wozniak A, Li H, Gebreyohannes YK, Wellens J, Hompes D, et al. Anti-tumor activity of the MDM2-TP53 inhibitor BI-907828 in dedifferentiated liposarcoma patient-derived xenograft models harboring MDM2 amplification. *Clin Transl Oncol*. 2020;22(4):546-54.
11. Lee A, Huang P, DeMatteo RP, and Pollack SM. Immunotherapy for Soft Tissue Sarcoma: Tomorrow Is Only a Day Away. *Am Soc Clin Oncol Educ Book*. 2016;35:281-90.
12. Petitprez F, de Reynies A, Keung EZ, Chen TW, Sun CM, Calderaro J, et al. B cells are associated with survival and immunotherapy response in sarcoma. *Nature*. 2020;577(7791):556-60.
13. Pollack SM, He Q, Yearley JH, Emerson R, Vignali M, Zhang Y, et al. T-cell infiltration and clonality correlate with programmed cell death protein 1 and programmed death-ligand 1 expression in patients with soft tissue sarcomas. *Cancer*. 2017;123(17):3291-304.
14. Roland CL, Nassif Haddad EF, Keung EZ, Wang WL, Lazar AJ, Lin H, et al. A randomized, non-comparative phase 2 study of neoadjuvant immune-checkpoint blockade in retroperitoneal dedifferentiated liposarcoma and extremity/truncal undifferentiated pleomorphic sarcoma. *Nat Cancer*. 2024.
15. Tawbi HA, Burgess M, Bolejack V, Van Tine BA, Schuetze SM, Hu J, et al. Pembrolizumab in advanced soft-tissue sarcoma and bone sarcoma (SARC028): a multicentre, two-cohort, single-arm, open-label, phase 2 trial. *Lancet Oncol*. 2017;18(11):1493-501.
16. Keung EZ, Burgess M, Salazar R, Parra ER, Rodrigues-Canales J, Bolejack V, et al. Correlative Analyses of the SARC028 Trial Reveal an Association Between Sarcoma-Associated Immune Infiltrate and Response to Pembrolizumab. *Clin Cancer Res*. 2020;26(6):1258-66.

17. Helmink BA, Reddy SM, Gao J, Zhang S, Basar R, Thakur R, et al. B cells and tertiary lymphoid structures promote immunotherapy response. *Nature*. 2020;577(7791):549-55.
18. Kersten K, de Visser KE, van Miltenburg MH, and Jonkers J. Genetically engineered mouse models in oncology research and cancer medicine. *EMBO Mol Med*. 2017;9(2):137-53.
19. Franklin MR, Platero S, Saini KS, Curigliano G, and Anderson S. Immuno-oncology trends: preclinical models, biomarkers, and clinical development. *J Immunother Cancer*. 2022;10(1).
20. Cancer Genome Atlas Research Network. Electronic address edsc, and Cancer Genome Atlas Research N. Comprehensive and Integrated Genomic Characterization of Adult Soft Tissue Sarcomas. *Cell*. 2017;171(4):950-65 e28.
21. Assi T, Kattan J, Rassy E, Nassereddine H, Farhat F, Honore C, et al. Targeting CDK4 (cyclin-dependent kinase) amplification in liposarcoma: A comprehensive review. *Crit Rev Oncol Hematol*. 2020;153:103029.
22. Traweek RS, Cope BM, Roland CL, Keung EZ, Nassif EF, and Erstad DJ. Targeting the MDM2-p53 pathway in dedifferentiated liposarcoma. *Front Oncol*. 2022;12:1006959.
23. Italiano A, Bianchini L, Keslair F, Bonnafous S, Cardot-Leccia N, Coindre JM, et al. HMGA2 is the partner of MDM2 in well-differentiated and dedifferentiated liposarcomas whereas CDK4 belongs to a distinct inconsistent amplicon. *Int J Cancer*. 2008;122(10):2233-41.
24. Puzio-Kuter AM, Laddha SV, Castillo-Martin M, Sun Y, Cordon-Cardo C, Chan CS, et al. Involvement of tumor suppressors PTEN and p53 in the formation of multiple subtypes of liposarcoma. *Cell Death Differ*. 2015;22(11):1785-91.
25. Hernando E, Charytonowicz E, Dudas ME, Menendez S, Matushansky I, Mills J, et al. The AKT-mTOR pathway plays a critical role in the development of leiomyosarcomas. *Nat Med*. 2007;13(6):748-53.
26. Uhrig-Schmidt S, Geiger M, Luippold G, Birk G, Mennerich D, Neubauer H, et al. Gene delivery to adipose tissue using transcriptionally targeted rAAV8 vectors. *PLoS One*. 2014;9(12):e116288.
27. Bates R, Huang W, and Cao L. Adipose Tissue: An Emerging Target for Adeno-associated Viral Vectors. *Mol Ther Methods Clin Dev*. 2020;19:236-49.
28. Romanelli SM, and MacDougald OA. Viral and Nonviral Transfer of Genetic Materials to Adipose Tissues: Toward a Gold Standard Approach. *Diabetes*. 2020;69(12):2581-8.
29. Gagneten S, Le Y, Miller J, and Sauer B. Brief expression of a GFP cre fusion gene in embryonic stem cells allows rapid retrieval of site-specific genomic deletions. *Nucleic Acids Res*. 1997;25(16):3326-31.
30. Kaspar BK, Vissel B, Bengoechea T, Crone S, Randolph-Moore L, Muller R, et al. Adeno-associated virus effectively mediates conditional gene modification in the brain. *Proc Natl Acad Sci U S A*. 2002;99(4):2320-5.
31. Crago AM, Socci ND, DeCarolis P, O'Connor R, Taylor BS, Qin LX, et al. Copy number losses define subgroups of dedifferentiated liposarcoma with poor prognosis and genomic instability. *Clin Cancer Res*. 2012;18(5):1334-40.
32. Beird HC, Wu CC, Ingram DR, Wang WL, Alimohamed A, Gumbs C, et al. Genomic profiling of dedifferentiated liposarcoma compared to matched well-differentiated liposarcoma reveals higher genomic complexity and a common origin. *Cold Spring Harb Mol Case Stud*. 2018;4(2).
33. Agaram NP. Update on Myogenic Sarcomas. *Surg Pathol Clin*. 2019;12(1):51-62.
34. Dermawan JK, Hwang S, Wexler L, Tap WD, Singer S, Vanderbilt CM, et al. Myxoid pleomorphic liposarcoma is distinguished from other liposarcomas by widespread loss of heterozygosity and significantly worse overall survival: a genomic and clinicopathologic study. *Mod Pathol*. 2022;35(11):1644-55.

35. Harms PW, Verhaegen ME, Hu K, Hrycaj SM, Chan MP, Liu CJ, et al. Genomic evidence suggests that cutaneous neuroendocrine carcinomas can arise from squamous dysplastic precursors. *Mod Pathol*. 2022;35(4):506-14.
36. Angeles CV, Velez A, Rios J, Laxa B, Shum D, Ruiz PD, et al. A High-Content Screen for C/EBPalpha Expression Identifies Novel Therapeutic Agents in Dedifferentiated Liposarcoma. *Clin Cancer Res*. 2022;28(1):175-86.
37. Hsu JY, Seligson ND, Hays JL, Miles WO, and Chen JL. Clinical Utility of CDK4/6 Inhibitors in Sarcoma: Successes and Future Challenges. *JCO Precis Oncol*. 2022;6:e2100211.
38. Rosen ED, Hsu CH, Wang X, Sakai S, Freeman MW, Gonzalez FJ, et al. C/EBPalpha induces adipogenesis through PPARgamma: a unified pathway. *Genes Dev*. 2002;16(1):22-6.
39. Koschmieder S, Halmos B, Levantini E, and Tenen DG. Dysregulation of the C/EBPalpha differentiation pathway in human cancer. *J Clin Oncol*. 2009;27(4):619-28.
40. Nebenfuehr S, Kollmann K, and Sexl V. The role of CDK6 in cancer. *Int J Cancer*. 2020;147(11):2988-95.
41. Papenfuss AT, and Thomas DM. The life history of neochromosomes revealed. *Mol Cell Oncol*. 2015;2(4):e1000698.
42. Gobble RM, Qin LX, Brill ER, Angeles CV, Ugras S, O'Connor RB, et al. Expression profiling of liposarcoma yields a multigene predictor of patient outcome and identifies genes that contribute to liposarcomagenesis. *Cancer Res*. 2011;71(7):2697-705.
43. Wu YV, Okada T, DeCarolis P, Socci N, O'Connor R, Geha RC, et al. Restoration of C/EBPalpha in dedifferentiated liposarcoma induces G2/M cell cycle arrest and apoptosis. *Genes Chromosomes Cancer*. 2012;51(4):313-27.
44. McGue JJ, Edwards JJ, Griffith BD, and Frankel TL. Multiplex Fluorescent Immunohistochemistry for Preservation of Tumor Microenvironment Architecture and Spatial Relationship of Cells in Tumor Tissues. *Methods Mol Biol*. 2023;2660:235-46.
45. Harms PW, Frankel TL, Moutafi M, Rao A, Rimm DL, Taube JM, et al. Multiplex Immunohistochemistry and Immunofluorescence: A Practical Update for Pathologists. *Mod Pathol*. 2023;36(7):100197.
46. Sun L, Verhaegen ME, McGue J, Olivei AC, Dlugosz AA, Frankel TL, et al. Development of a Multiplex Immunofluorescence Assay for Tumor Microenvironment Studies of Human and Murine Merkel Cell Carcinoma. *Lab Invest*. 2024;104(10):102128.
47. Petitprez F, Levy S, Sun CM, Meylan M, Linhard C, Becht E, et al. The murine Microenvironment Cell Population counter method to estimate abundance of tissue-infiltrating immune and stromal cell populations in murine samples using gene expression. *Genome Med*. 2020;12(1):86.
48. Jiang X, Clark RA, Liu L, Wagers AJ, Fuhlbrigge RC, and Kupper TS. Skin infection generates non-migratory memory CD8+ T(RM) cells providing global skin immunity. *Nature*. 2012;483(7388):227-31.
49. Liu L, Zhong Q, Tian T, Dubin K, Athale SK, and Kupper TS. Epidermal injury and infection during poxvirus immunization is crucial for the generation of highly protective T cell-mediated immunity. *Nat Med*. 2010;16(2):224-7.
50. Zhu J, Peng T, Johnston C, Phasouk K, Kask AS, Klock A, et al. Immune surveillance by CD8alphaalpha+ skin-resident T cells in human herpes virus infection. *Nature*. 2013;497(7450):494-7.
51. Han J, Zhao Y, Shirai K, Molodtsov A, Kolling FW, Fisher JL, et al. Resident and circulating memory T cells persist for years in melanoma patients with durable responses to immunotherapy. *Nat Cancer*. 2021;2(3):300-11.

52. Savas P, Virassamy B, Ye C, Salim A, Mintoff CP, Caramia F, et al. Single-cell profiling of breast cancer T cells reveals a tissue-resident memory subset associated with improved prognosis. *Nat Med*. 2018;24(7):986-93.
53. Guo X, Zhang Y, Zheng L, Zheng C, Song J, Zhang Q, et al. Global characterization of T cells in non-small-cell lung cancer by single-cell sequencing. *Nat Med*. 2018;24(7):978-85.
54. Menares E, Galvez-Cancino F, Caceres-Morgado P, Ghorani E, Lopez E, Diaz X, et al. Tissue-resident memory CD8(+) T cells amplify anti-tumor immunity by triggering antigen spreading through dendritic cells. *Nat Commun*. 2019;10(1):4401.
55. Park SL, Buzzai A, Rautela J, Hor JL, Hochheiser K, Effern M, et al. Tissue-resident memory CD8(+) T cells promote melanoma-immune equilibrium in skin. *Nature*. 2019;565(7739):366-71.
56. Malik BT, Byrne KT, Vella JL, Zhang P, Shabaneh TB, Steinberg SM, et al. Resident memory T cells in the skin mediate durable immunity to melanoma. *Sci Immunol*. 2017;2(10).
57. Ganesan AP, Clarke J, Wood O, Garrido-Martin EM, Chee SJ, Mellows T, et al. Tissue-resident memory features are linked to the magnitude of cytotoxic T cell responses in human lung cancer. *Nat Immunol*. 2017;18(8):940-50.
58. Kumar BV, Ma W, Miron M, Granot T, Guyer RS, Carpenter DJ, et al. Human Tissue-Resident Memory T Cells Are Defined by Core Transcriptional and Functional Signatures in Lymphoid and Mucosal Sites. *Cell Rep*. 2017;20(12):2921-34.
59. Workel HH, Komdeur FL, Wouters MC, Plat A, Klip HG, Eggink FA, et al. CD103 defines intraepithelial CD8+ PD1+ tumour-infiltrating lymphocytes of prognostic significance in endometrial adenocarcinoma. *Eur J Cancer*. 2016;60:1-11.
60. Schenkel JM, and Masopust D. Tissue-resident memory T cells. *Immunity*. 2014;41(6):886-97.
61. Chen ZY, Wang L, Gu L, Qu R, Lowrie DB, Hu Z, et al. Decreased Expression of CD69 on T Cells in Tuberculosis Infection Resisters. *Front Microbiol*. 2020;11:1901.
62. Dowlatshahi M, Huang V, Gehad AE, Jiang Y, Calarese A, Teague JE, et al. Tumor-specific T cells in human Merkel cell carcinomas: a possible role for Tregs and T-cell exhaustion in reducing T-cell responses. *J Invest Dermatol*. 2013;133(7):1879-89.
63. Matushansky I, Hernando E, Socci ND, Matos T, Mills J, Edgar MA, et al. A developmental model of sarcomagenesis defines a differentiation-based classification for liposarcomas. *Am J Pathol*. 2008;172(4):1069-80.
64. Fridman WH, Meylan M, Petitprez F, Sun CM, Italiano A, and Sautes-Fridman C. B cells and tertiary lymphoid structures as determinants of tumour immune contexture and clinical outcome. *Nat Rev Clin Oncol*. 2022.
65. Olson B, Li Y, Lin Y, Liu ET, and Patnaik A. Mouse Models for Cancer Immunotherapy Research. *Cancer Discov*. 2018;8(11):1358-65.
66. Buque A, and Galluzzi L. Modeling Tumor Immunology and Immunotherapy in Mice. *Trends Cancer*. 2018;4(9):599-601.
67. Han J, Khatwani N, Searles TG, Turk MJ, and Angeles CV. Memory CD8(+) T cell responses to cancer. *Semin Immunol*. 2020;49:101435.
68. Van Gassen S, Callebaut B, Van Helden MJ, Lambrecht BN, Demeester P, Dhaene T, et al. FlowSOM: Using self-organizing maps for visualization and interpretation of cytometry data. *Cytometry A*. 2015;87(7):636-45.
69. Gattinoni L, Speiser DE, Lichterfeld M, and Bonini C. T memory stem cells in health and disease. *Nat Med*. 2017;23(1):18-27.
70. Velikkakam T, Gollob KJ, and Dutra WO. Double-negative T cells: Setting the stage for disease control or progression. *Immunology*. 2022;165(4):371-85.
71. Molodtsov A, and Turk MJ. Tissue Resident CD8 Memory T Cell Responses in Cancer and Autoimmunity. *Front Immunol*. 2018;9:2810.

72. Dou A, and Fang J. Heterogeneous Myeloid Cells in Tumors. *Cancers (Basel)*. 2021;13(15).
73. Fridman WH, Meylan M, Pupier G, Calvez A, Hernandez I, and Sautes-Fridman C. Tertiary lymphoid structures and B cells: An intratumoral immunity cycle. *Immunity*. 2023;56(10):2254-69.
74. DeNardo DG, and Ruffell B. Macrophages as regulators of tumour immunity and immunotherapy. *Nat Rev Immunol*. 2019;19(6):369-82.
75. Dancsok AR, Gao D, Lee AF, Steigen SE, Blay JY, Thomas DM, et al. Tumor-associated macrophages and macrophage-related immune checkpoint expression in sarcomas. *Oncoimmunology*. 2020;9(1):1747340.
76. Dancsok AR, Setsu N, Gao D, Blay JY, Thomas D, Maki RG, et al. Expression of lymphocyte immunoregulatory biomarkers in bone and soft-tissue sarcomas. *Mod Pathol*. 2019;32(12):1772-85.
77. Balachandran VP, Luksza M, Zhao JN, Makarov V, Moral JA, Remark R, et al. Identification of unique neoantigen qualities in long-term survivors of pancreatic cancer. *Nature*. 2017;551(7681):512-6.
78. Laroche-Clary A, Chaire V, Algeo MP, Derieppe MA, Loarer FL, and Italiano A. Combined targeting of MDM2 and CDK4 is synergistic in dedifferentiated liposarcomas. *J Hematol Oncol*. 2017;10(1):123.
79. Bill KL, Garnett J, Meaux I, Ma X, Creighton CJ, Bolshakov S, et al. SAR405838: A Novel and Potent Inhibitor of the MDM2:p53 Axis for the Treatment of Dedifferentiated Liposarcoma. *Clin Cancer Res*. 2016;22(5):1150-60.
80. Wang S, Sun W, Zhao Y, McEachern D, Meaux I, Barriere C, et al. SAR405838: an optimized inhibitor of MDM2-p53 interaction that induces complete and durable tumor regression. *Cancer Res*. 2014;74(20):5855-65.
81. Choi JH, Yu NK, Baek GC, Bakes J, Seo D, Nam HJ, et al. Optimization of AAV expression cassettes to improve packaging capacity and transgene expression in neurons. *Mol Brain*. 2014;7:17.
82. Hsu SM, Raine L, and Fanger H. Use of avidin-biotin-peroxidase complex (ABC) in immunoperoxidase techniques: a comparison between ABC and unlabeled antibody (PAP) procedures. *J Histochem Cytochem*. 1981;29(4):577-80.
83. Belkina AC, Ciccolella CO, Anno R, Halpert R, Spidlen J, and Snyder-Cappione JE. Automated optimized parameters for T-distributed stochastic neighbor embedding improve visualization and analysis of large datasets. *Nat Commun*. 2019;10(1):5415.
84. Becton DaC. Ashland, OR: BD Life Sciences; 2023.
85. Hanzelmann S, Castelo R, and Guinney J. GSVA: gene set variation analysis for microarray and RNA-seq data. *BMC Bioinformatics*. 2013;14:7.